Surv Geophys (2014) 35:681–722
DOI 10.1007/s10712-013-9244-0

Sea Surface Salinity Observations from Space with the SMOS Satellite: A New Means to Monitor the Marine Branch of the Water Cycle

Nicolas Reul · Severine Fournier · Jaqueline Boutin · Olga Hernandez · Christophe Maes · Bertrand Chapron · Gaël Alory · Yves Quilfen · Joseph Tenerelli · Simmon Morisset · Yann Kerr · Susanne Mecklenburg · Steven Delwart

Received: 21 January 2013 / Accepted: 18 June 2013 / Published online: 8 August 2013

Abstract While it is well known that the ocean is one of the most important component of the climate system, with a heat capacity 1,100 times greater than the atmosphere, the ocean is also the primary reservoir for freshwater transport to the atmosphere and largest component of the global water cycle. Two new satellite sensors, the ESA Soil Moisture and Ocean Salinity (SMOS) and the NASA Aquarius SAC-D missions, are now providing the first space-borne measurements of the sea surface salinity (SSS). In this paper, we present examples demonstrating how SMOS-derived SSS data are being used to better characterize

N. Reul · S. Fournier · B. Chapron · Y. Quilfen
Laboratoire d'Océanographie Spatiale, Institut Français de recherche et d'Exploitation de la Mer, Centre Bretagne BP 70, 29280 Plouzané, France

N. Reul (✉)
Centre Méditerranée, Zone Portuaire de Brégaillon, BP 330, 83507 La Seyne-sur-Mer Cedex, France
e-mail: nreul@ifremer.fr

J. Boutin · O. Hernandez · S. Morisset
Laboratoire d'Océanographie et du Climat: Expérimentation et Approches Numériques, UMR 7159 CNRS/UPMC/IRD/MNHN, Paris, France

C. Maes · G. Alory
LEGOS, OMP, CNAP, Université de Toulouse, Toulouse, France

J. Tenerelli
CLS-Radar Division, Bâtiment Le Ponant, Avenue La Pérouse, Technopôle Brest-Iroise, 29280 Plouzané, France

Y. Kerr
CESBIO, Toulouse, France

S. Mecklenburg · S. Delwart
ESA-ESRIN, Frascatti, Italy

key land–ocean and atmosphere–ocean interaction processes that occur within the marine hydrological cycle. In particular, SMOS with its ocean mapping capability provides observations across the world's largest tropical ocean fresh pool regions, and we discuss from intraseasonal to interannual precipitation impacts as well as large-scale river runoff from the Amazon–Orinoco and Congo rivers and its offshore advection. Synergistic multi-satellite analyses of these new surface salinity data sets combined with sea surface temperature, dynamical height and currents from altimetry, surface wind, ocean color, rainfall estimates, and in situ observations are shown to yield new freshwater budget insight. Finally, SSS observations from the SMOS and Aquarius/SAC-D sensors are combined to examine the response of the upper ocean to tropical cyclone passage including the potential role that a freshwater-induced upper ocean barrier layer may play in modulating surface cooling and enthalpy flux in tropical cyclone track regions.

Keywords Sea surface salinity · SMOS satellite · Passive microwave remote sensing · Oceanic freshwater cycle

1 Introduction

Salinity is known to play an important role in the dynamics of the ocean's thermohaline overturning circulation and in large-scale atmosphere–ocean climate signals such as the El Nino Southern Oscillation (ENSO), and is the key freshwater tracer within the oceanic component of the global hydrologic cycle, a branch that comprises most of the global precipitation and evaporation as well as the river runoff (Schmitt 2008). Multi-decadal sea surface salinity (SSS) trends have been documented in tropical and high latitudes and associated with signatures of evaporation or precipitation variation that are consistent with global warming scenarios (e.g., Dickson et al. 2002; Gordon and Guilivi 2008; Morrow et al. 2008; Cravatte et al. 2009; Yu 2011; Durack et al. 2012; Terray et al. 2011). These studies highlight the need for well-sampled SSS time series both for monitoring the change and to improve the basic understanding of the respective roles of the atmosphere and ocean dynamics, thermodynamics, air–sea interaction, and land–ocean interaction in the global water cycle context.

Our basic knowledge of the global SSS distribution is derived from the compilations of all available oceanographic data collected over time (e.g., Boyer and Levitus 2002). The SSS in situ observing system has expanded significantly during the last decade due mostly to the full deployment of the Argo profiling float array and now provides a monthly SSS estimate on a grid of roughly 300–400 km^2. Notwithstanding these recent gains, this sampling density is still too sparse to resolve climatologically important intraseasonal, seasonal, and interannual to decadal signals at the 300-km spatial scale within which SSS is known to vary significantly (Lagerloef et al. 2010). The recent launches of the ESA/Soil Moisture and Ocean Salinity (SMOS, see Kerr et al. 2010; Font et al. 2010) and NASA/Aquarius SAC-D (Lagerloef et al. 2008; Lagerloef 2012) mission satellites represent contributions toward filling this gap using passive microwave remote sensing.

Salinity remote sensing is based on the measurement of sea surface microwave emission at the lower end of the microwave spectrum and from a surface skin layer having a thickness of O(1 cm). This emission depends partly on the dielectric constant of sea water, which in turn can be related to salinity and temperature. Thus, given sea surface temperature (SST), theory predicts some ability to invert SSS information. In practice, however, numerous additional external factors (extra-terrestrial sources, atmosphere, ionosphere, and surface roughness) also contribute to the satellite-observed emission, and these must be corrected to allow accurate ocean salinity estimates. The SMOS and Aquarius sensors are both ocean microwave radiometers operating at a frequency of ~ 1.4 GHz (L-band, wavelength of 21 cm), a band chosen for the relatively strong sensitivity to change in salinity and because this is a transmission-free, or protected, frequency. An additional and important benefit for this choice is minimization of atmospheric signal contributions.

Based on the observed SSS variability and need to better resolve it, the satellite missions aim to produce salinity estimates with an accuracy of 0.1–0.2 over the so-called Global Ocean Data Assimilation Experiment scales of 100 km, 1 month or 200 km, and 10 days. This is a challenging objective for several reasons. First, the sensitivity of L-band brightness temperatures to variations in SSS is on average 0.5 degK per salinity scale. This sensitivity is very weak given that spatial and temporal variability in open ocean SSS does not exceed several units and that the instrument noise is typically 2–5 degK. Note that salinity computations are based on the Practical Salinity Scale PSS-78 and reported with no units (United Nations Educational, Scientific and Cultural Organization 1985). Second, there are many geophysical sources of brightness at L-band that corrupt the salinity signal, and correction models for these factors have uncertain accuracy. Moreover, the technical approach developed in order to achieve adequate radiometric accuracy and spatiotemporal resolution for SMOS is polarimetric interferometric radiometry, the first such space-borne system. The complex SMOS image reconstruction data processing includes contamination by different errors and induces residual inaccuracies in SSS estimates. Finally, there is significant radio frequency interference emanating from sources along the many coastlines that contaminate data collected over many ocean regions. Nevertheless, much work at ESA SMOS level 2 expert centers and the CNES/IFREMER Centre Aval de Traitement des Données SMOS (CATDS) has addressed these issues, leading to the first global satellite SSS estimates (Font et al. 2013; Reul et al. 2012; Boutin et al. 2012a).

Two examples of monthly composite SMOS SSS maps are shown in Fig. 1. They show salient basin scale features, including the elevated salinity in the Atlantic relative to the other basins, and the general correspondence of lower SSS with known river runoff and tropical precipitation regions. SMOS data validation efforts using in situ observations reveal an overall SSS accuracy on the order of 0.3 (Boutin et al. 2012a; Reul et al. 2012; Banks et al. 2012; Font et al. 2013), but with degraded quality at high latitudes partly because of reduced sensitivity in colder waters. While further improvements are in progress, many interesting features of the global SSS could be already evidenced.

This paper reviews preliminary results addressing several key applications of these new satellite SSS data. Given the reduced SMOS sensitivity in cold waters, the focus is on tropical ocean data where SMOS measurements have proven to be the most accurate. We also attempt to highlight combined use of other satellite and in situ observations (altimetry, SST, ocean color, river discharge, evaporation, and precipitation). It is shown that these new data are proving useful in the monitoring of intraseasonal to interannual variability across major tropical freshwater pools of the world ocean. SMOS-detected SSS freshening events within intense precipitation zones (e.g., the Inter Tropical Convergence Zone) are also shown to provide promising new information related to the ocean surface response to rainfall. Finally, SMOS SSS data are used to address interactions between wind-driven phenomena, such as upwelling and tropical cyclones (TCs), and some of the world's largest fresh pools. The data sets used in these cases are described in Sect. 2. SMOS monitoring capabilities for the major tropical river plumes are given in Sect. 3. In Sects. 4 and 5, we illustrate rain impacts detected in SMOS SSS data; then, their application improved the understanding of freshwater pools interaction with the atmosphere. Conclusions and perspectives are given in Sect. 6.

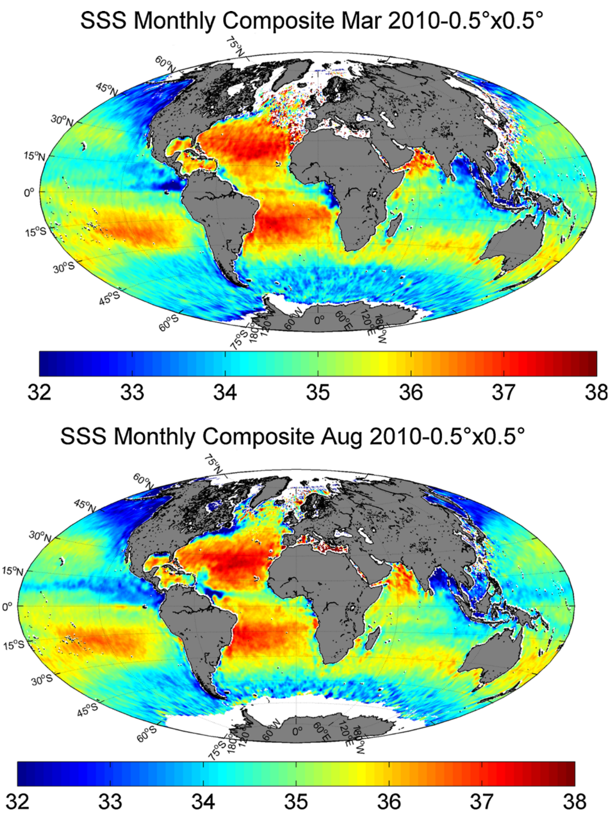

Fig. 1 Monthly composites of the sea surface salinity at a spatial resolution of 0.5° × 0.5° deduced from SMOS data (CATDS v2) for the months of March (*Upper*) and August (*Lower*) 2010

2 Data

A range of satellite and in situ data sets are used in the present study with focus on the years 2010–2012 following the SMOS launch date. The data products are described below.

2.1 SMOS SSS Data

SMOS (Soil Moisture and Ocean Salinity) is the European Space Agency (ESA)'s water mission (Kerr et al. 2010; Mecklenburg et al. 2012), an Earth Explorer Opportunity Mission approved under the Living Planet Program. SMOS was launched in November 2009, and the technical approach developed to achieve adequate radiometric accuracy, as well as spatial and temporal resolution compromising between land and ocean science requirements, is polarimetric interferometric radiometry (Ruf et al. 1988; Font et al. 2010) at L-band (frequency of ~1.4 GHz). ESA produces so-called level 2 SSS, or L2 products, which correspond to instantaneous SSS retrievals under the satellite swath.

In the present study, level 2 SMOS SSS are from the first SMOS/ESA annual reprocessing campaign in which ESA level 1 v5.04 and level 2 v5.50 processors have been used. In these versions, significant improvements with respect to the flaws discovered in the first products (e.g., Reul et al. 2012) have been implemented (see a complete description in the Algorithm Theoretical Basis Document (ATBD) available at http://www.argans.co.uk/smos/docs/deliverables/). Nevertheless, accuracy of these instantaneous SSS retrievals is rather low (~0.6–1.7), and space–time averaging of the level 2 products is needed (so-called level 3 SSS) to decrease the noise level in the retrievals.

Here, we used two types of composite SSS level 3 products generated in laboratories participating to the Expertise Center of the Centre Aval de Traitement des Données SMOS (CATDS, http://www.catds.fr), which is the French ground segment for the SMOS data. These products are built either from ESA level 1 products (Reul and Tenerelli 2011) or from ESA level 2 products (Boutin et al. 2012b).

These research products aim at assessing the quality of SMOS operational products (ESA level 2 and CATDS-OP level 3) and at studying new processing to be implemented in the future in operational chains. Main characteristics of these products are detailed in Table 1. CEC-IFREMER products have been used in Sects. 3, and 5, CEC-LOCEAN products in Sect. 4.

Overall accuracy of the 10-day composite products at 25-km resolution is on the order of 0.3 practical salinity scale in the tropical oceans (Reul and Tenerelli 2011).

2.2 Ocean Surface Currents

Here, we used the 1/3° resolution global surface current products from Ocean Surface Current Analyses Real time (OSCAR) (Bonjean and Lagerloef 2002; http://www.oscar.noaa.gov), directly calculated from satellite altimetry and ocean vector winds.

Table 1 Summary of characteristics of CATDS-CEC SSS level 3 products

	CEC-IFREMER	CEC-LOCEAN
SSS retrieval method	SSS retrieved from first Stokes parameter (Reul and Tenerelli 2011)	SSS retrieved from polarized Tbs along dwell lines using an iterative retrieval (see ESA L2OS ATBD)
Region of the instrument field of view (FOV) considered for SSS retrieval	Alias free field of view only	Alias free field of view (AFFOV) and extended AFFOV along dwell lines with at least 130 Tb data samples in AFFOV (~±300 km from the swath center)
Tb filtering method	Determined from interorbit consistency in incidence angles classes and thresholding	Determined from consistency along dwell lines as reported in ESA level 2 products
Galactic model	Geometrical optics model	Kirchoff's approx. scattering at 3 m/s
Roughness/foam models	Empirical adjustment of Tb dependencies to wind speed	Empirical adjustment of parameters in roughness model and foam coverage models (Yin et al. 2012)
Calibration	Single ocean target transformation (OTT) + daily 5° × 5° adjustment wrt World Ocean 2001 SSS climatology	Variable OTT (every 2 weeks synchronized with noise injection radiometer as defined in ESA reprocessing)
Average	Simple average	Average weighted by theoretical error on retrieved SSS and spatial resolution

The OSCAR data processing system calculates sea surface velocities from satellite altimetry (AVISO), vector wind fields (QuikSCAT), as well as from sea surface temperature (Reynolds–Smith) using quasi-steady geostrophic, local wind-driven, and thermal wind dynamics. Near real-time velocities are calculated both on a $1° \times 1°$ and $1/3° \times 1/3°$ grid and on a $\sim$5-day time base over the global ocean. Surface currents are provided on the OSCAR Web site (http://www.oscar.noaa.gov) starting from 1992 along with validations with drifters and moorings. The 1/3° resolution is available for FTP download through ftp://esr.org/pub/datasets/SfcCurrents/ThirdDegree.

2.3 Rain, Evaporation and River Discharge Data

To estimate the rain rate over the oceans, we used three different satellite products.

One is the monthly Tropical Rainfall Measuring Mission (TRMM) Composite Climatology (TCC) of surface precipitation based on 13 years of data from the TRMM. The TCC takes advantage of the information from multiple estimates of precipitation from TRMM to construct mean value maps over the tropics (36°N–36°S) for each month of the year at 0.5° latitude–longitude resolution. The first-time use of both active and passive microwave instruments on board TRMM has made it the foremost satellite for the study of precipitation in the tropics and has led to a better understanding of the underlying physics and distribution of precipitation in this region. The products are available at NASA Goddard Space Flight Center Global Change Master Directory (http://gcmd.nasa.gov).

The second type of satellite rain rate estimates that we used in the present study are the so-called "TRMM and Other Satellites" (3B42) products, obtained through the NASA/Giovanni server (http://reason.gsfc.nasa.gov/OPS/Giovanni). The 3B42 estimates are 3 hourly at a spatial resolution of 0.25° with spatial extent covering a global belt (−180°W–180°E) extending from 50°S to 50°N latitude. The major inputs into the 3B42 algorithm are IR data from geostationary satellites and Passive Microwave data from the TRMM microwave imager (TMI), special sensor microwave imager (SSM/I), Advanced Microwave Sounding Unit (AMSU), and Advanced Microwave Sounding Radiometer-Earth Observing System (AMSR-E).

The Special Sensor Microwave Imager (SSM/I) F16 and F17 orbits cross SMOS orbits within −20 min and +40 min. Hence, numerous SMOS level 2 are collocated with SSMI rain rates (RR) within this range of time. In addition to the TRMM 3B42 products, we therefore used SSM/Is data sets to perform colocations between SMOS SSS and rain estimates. SSM/Is RR version 7 was used and downloaded from http://www.remss.com.

The evaporation (E) data set was taken from the version 3 products of the Objectively Analyzed air-sea Fluxes (OAFlux) project (Yu and Weller 2007).

Finally, the discharge data for the Amazon, Orinoco, and Congo rivers were obtained from the Environmental Research Observatory HYBAM (geodynamical, hydrological, and biogeochemical control of erosion/alteration and material transport in the Amazon basin) Web site (http://www.ore-hybam.org/).

2.4 Ocean Color Products

To study the spatiotemporal coherency between SSS signals from some major tropical river plumes and ocean color properties, we used the level 3 daily, 4-km resolution estimates of the absorption coefficient of colored detrital matter (CDM) at 443 nm. These products processed and distributed by ACRI-ST GlobColour service are supported by the EU FP7 MyOcean2 and the ESA GlobColour Projects, using ESA ENVISAT MERIS data, NASA MODIS and SeaWiFS data. These products have been averaged at the SMOS L3 product 0.25° resolution, with a 10-day running mean.

2.5 In Situ Data

Salinity measurements from Argo floats are provided by the Coriolis data center (http://www.coriolis.eu.org/). The upper ocean salinity values recorded between 4- and 10-m depth will be referred to as Argo SSS following Boutin et al. (2012b).

Global SSS maps are derived from delayed time quality checked in situ measurements (Argo and ship) by IFREMER/LPO, Laboratoire de Physique des Oceans, using the In Situ Analysis System (ISAS) optimal interpolation (D7CA2S0 re-analysis product) (see a method description on http://wwz.ifremer.fr/lpo/SO-Argo-France/Products/Global-Ocean-T-S/Monthly-fields-2004-2010 and in (Gaillard et al. 2009)). The choice for the time and space scales used in that method results from a compromise between what is known of ocean time and space scales and what can actually be resolved with the Argo array (3°, 10 days); two length scales are considered: the first one is isotropic and equal to 300 km, the second one is set equal to 4 times the average Rossby radius of deformation of the area. As a result, we expect these maps being smoother, especially in tropical areas, than SMOS SSS maps averaged over 0.25° × 0.25° or 1° × 1°.

3 SMOS Monitoring of the Major Tropical Atlantic River Plumes

Rivers are important variables in oceanography as their freshwater affects SSS and the buoyancy of the surface layer, and they represent a source of materials exotic to the ocean and important to biological activity. Obviously, they are key hydrologic components of the freshwater exchanges between land and ocean. Despite this importance, tracing major tropical river water (e.g., Amazon, Congo, and Ganges) over large distances has not been straightforward previously principally because of a lack of SSS observations. Tracing those very large rivers over great distances now become an important endeavor, as sufficient data are available from surface salinity sensors placed aboard satellites.

Occurrence of patches of low surface salinity (<35 practical salinity scales) in the tropical Atlantic Ocean is closely related to the presence of the mouths of the world's largest rivers in terms of freshwater discharge (e.g., Amazon, Congo, and Orinoco) and their subsequent spreading of freshwater by the upper ocean circulation. Another key freshwater source here is the Inter Tropical Convergence Zone (ITCZ), associated with relatively intense precipitation that migrates latitudinally over the tropical Atlantic throughout the year (Binet and Marchal 1993). One of these major low-salinity pools is formed by the Amazon and Orinoco river plumes spreading offshore from the South America northeastern coasts, and influencing a large fraction of the western tropical North Atlantic (Neumann 1969; Lentz 1995; Muller-Karger et al. 1988; Dessier and Donguy 1994). The Gulf of Guinea situated in the northeastern equatorial Atlantic is also an important location for the freshwater budget in the tropical Atlantic. It is a region of intense precipitation with as much as 30 cm of rain falling per month during the rainy season (Yoo and Carton 1988). Furthermore, into this area flows the Congo River, the largest freshwater input to any eastern ocean boundary. These large-scale low-salinity "lenses" at the tropical Atlantic surface can be traced over distances ranging from several hundred up to thousands of kilometers in the upper ocean. They are characterized by very distinct and in general strong seasonally varying spatial extents.

3.1 Amazon and Orinoco River Plume Monitoring

The Amazon is the world's largest river in terms of freshwater discharge (Milliman and Meade 1983; Perry et al. 1996). It drains a large fraction of the South American continent, discharging on average $1.55 \pm 0.13 \times 10^5$ m^3 s^{-1} of freshwater into the equatorial Atlantic Ocean (Perry et al.1996). This is about 15 % of the estimated global river discharge on an annual basis. The Amazon River is by far the largest single source of terrestrial freshwater to the ocean and contributes about 30 % of total river discharge to the Atlantic Ocean (Wisser et al. 2010). The structure of the Amazon plume is strongly influenced by a variety of physical processes, which are present on the northern Brazilian shelf: the North Brazil Current (Flagg et al. 1986; Richardson and McKee 1984), trade winds (Hellerman and Rosenstein 1983) and strong currents associated with the tide (Nittrouer and Demaster 1986). These physical processes play a very significant role in the dispersal and spreading of Amazon discharge (freshwater and suspended sediment) on the northern continental shelf of South America.

Previous studies have shown that Amazon plume water can be traced offshore and northwestward along the north Brazilian coast, covering most of the continental shelf from 11°S to 5°N (Muller-Karger et al. 1988, 1995) into the Caribbean (e.g., Steven and Brooks 1972; Froelich et al. 1978; Hellweger and Gordon 2002; Cherubin and Richardson 2007), and over 1,000 km eastward into the North Atlantic depending on the season. Beyond this region, the Amazon's water has been traced northwestward into the Caribbean Sea and eastward in the North Atlantic (Muller-Karger et al. 1988, 1995; Johns et al. 1990; Hellweger and Gordon 2002). Hydrographic surveys by Lentz and Limeburner (1995) revealed that the Amazon plume over the shelf is typically 3–10 m thick and between 80 and >200 km wide. Beyond the shelf, freshwater within the plume gradually attenuates with depth as it travels away from the source, with a penetration depth of 40–45 m as far as 2,600 km offshore (Hellweger and Gordon 2002; Hu et al. 2004).

Both chlorophyll (Chl) concentration and primary productivity are the greatest in the river plume–ocean transition zone, where the bulk of heavy sediments are deposited (Smith and Demaster 1996). The combination of riverine nutrient input and increased irradiance availability creates a highly productive transition zone, the location of which varies with the discharge from the river. High phytoplankton biomass and productivity of over 25 mg Chl-a m^{-3}and 8 g cm^{-2} day^{-1}, respectively, are found in this transition region (Smith and Demaster 1996). Because of this, the North Brazil shelf acts as a significant sink for atmospheric CO_2 (Ternon et al. 2000).

The northwestern tropical Atlantic is also an area where another major river in the world, the Orinoco, enters the ocean. The Orinoco River originates in the southern part of Venezuela and discharges waters from about 31 major and 2000 minor tributaries into the western tropical Atlantic. These waters are most of the time transported into the southeastern Caribbean sea, and during the rainy season, a larger but unquantified fraction of the plume also flows east around Trinidad and Tobago into the Caribbean. The Orinoco is considered to be the third largest river in the world in terms of volumetric discharge (after the Amazon and the Congo), discharging an average of $\sim 3.6 \times 10^4$ m^3 s^{-1} (Meade et al. 1983; Muller-Karger et al. 1989; Vörösmarty et al. 1998). Low discharge occurs during the dry season (January–May) and high discharge during the rainy season (July–October) as a result of the meridional migration of the ITCZ.

The freshwater discharges from the Amazon and Orinoco Rivers spread outward into the western equatorial Atlantic Ocean while continually mixing with surrounding salty ocean surface water. The averaged geographical distribution of the low-salinity signatures of the Amazon and Orinoco River plumes can be revealed with historical in situ surface salinity data. However, only satellite remote sensing data are known to provide means to monitor the wide surface dispersal of these two fresh pools, with ocean color data being the first to illustrate Amazon plume reach to well beyond 1,000 km (Muller-Karger et al. 1988). Since these first observations, the application of ocean color, altimetry, and SST satellite mapping in this region has increased in its sophistication, showing the ability to track surface plume area (e.g., Hu et al. 2004; Molleri et al. 2010), fronts along the shelf to the northwest (Baklouti et al. 2007), and northward propagating eddies or waves shed near the North Brazil Current (NBC) retro reflection region, the so-called NBC rings (Ffield 2005; Goni and Johns 2001; Garzoli et al. 2004). In each case, the satellite data are able to provide time-resolved information on advective processes up to certain limits that include cloud cover, minor SST and ocean color gradients, non-conservative dilution processes for the ocean color to salinity conversions (Salisbury et al. 2011), and baroclinicity and subgrid variability of the altimetry sea surface height anomaly tracking of the NBC rings. As first evidenced by Reul et al. 2009, passive remote sensing data at low microwave frequencies can be successively used to complement these more "classical" satellite observations to better follow the temporal evolution and spatial distribution of surface salinity within and adjacent to the Amazon River plume.

To illustrate this new capability, we first show in Fig. 2 comparisons between collocated SMOS SSS and in situ conductivity–temperature–depth (CTD) measurements acquired during the Geotraces West Atlantic cruise leg 2 across the Amazon River plume in June 2010. This campaign was conducted on RV Pelagia in the frame of the GEOTRACES international program (see http://www.geotraces.org/).

Comparison between satellite and 3-m depth in situ SSS data reveals an overall good agreement with a standard deviation of the difference SSS_{SMOS}–SSS_{CTD} of $\sim$0.45. In particular, the strong gradient and $\sim$3-unit drop observed as the R/V Pelagia leg crossed the Amazon River plume is well detected by the satellite observations.

New SSS products from satellite platforms such as SMOS allow in particular to gain insights into the advection pathways of the freshwater Amazon and Orinoco rivers plume along surface currents. For the first time, SMOS sampling capability thus enables imaging the plume structure almost every 3 days with a spatial resolution of about 40 km.

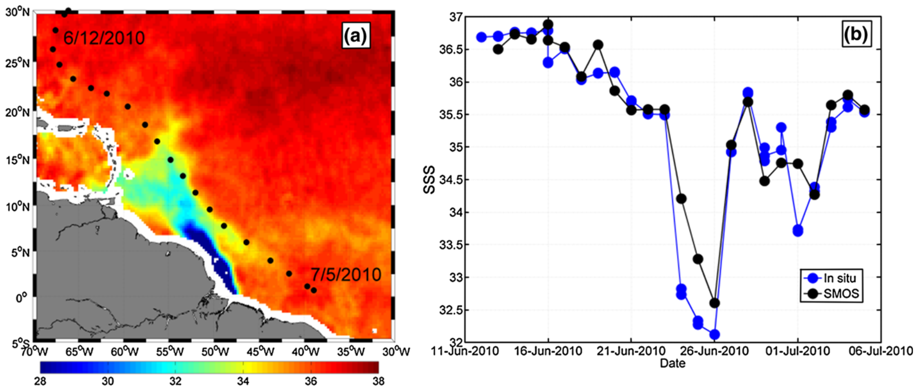

Fig. 2 **a** *Black dots*: location of the CTD stations conducted during the Geotraces West Atlantic cruise leg 2 (RV Pelagia) from 11 June to 5 July superimposed on the SMOS averaged SSS from June 12 to July 5, 2010. **b** Colocated surface salinity between SMOS and in situ data along the leg. SMOS data have been averaged at 50-km resolution with a ±5-day running temporal window

Combining SMOS SSS with altimeter-derived geostrophic currents and wind-driven (Ekman) estimated motions (Lagerloef et al. 1999), the advection of the spatial patterns of low salinity discharged from the major river mouths can now be analyzed systematically with an unprecedented resolution.

As illustrated by the Fig. 3 and by the animation available at http://www.ifremer.fr/naiad/salinityremotesensing.ifremer.fr/altimetry_amazon_atl.gif, a very good visual consistency is found between the geostrophic and Ekman surface current pattern estimates and the SMOS SSS spatiotemporal distribution along the year.

Mignot et al. (2007) show a long-term seasonal to monthly climatology that highlights two freshwater offshore pathways—the north passage to the warm pool and eastward entrainment into the North Equatorial Counter Current (NECC)—but they cannot clearly confirm or track this laterally with time in a given year.

SMOS SSS data combined with altimetry and surface wind information now enable to follow the spatiotemporal evolution of the plume along these two freshwater offshore pathways.

As illustrated in Fig. 3 (top), the surface freshwater dispersal patterns of the Amazon River plume are closely connected to the surface current topology derived from the merged altimeter and wind field product. As also evidenced earlier from several hydrographic surveys (e.g., Hellweger and Gordon 2002), it is clearly apparent in the satellite imagery that the NBC rings are key factors in modulating the freshwater pathways of the Amazon plume from the river mouth at the equator toward higher latitudes up to 20°–22°N.

Eastward entrainment of low-salinity water from the mouth of the Amazon River into the NECC is also evident in the SMOS data for the second half of the year 2010 (see Fig. 3, bottom). During that period, freshwater dispersal structure exhibits a zonal wavy pattern centered around $\sim$ 8°N induced by current instability waves shed near the NBC retroflection region (52°W, 8°N). To analyze the freshwater plume transport and the evolution of salinity along Lagrangian paths following such wavy patterns, hypothetical drifters were dropped around the mouth of the river at the beginning of June and temporally advected with the surface currents deduced from merged altimeter and wind products. The evolution of SSS from SMOS L-band and AMSR-E C-band sensors (see Reul et al. 2009 for details on the AMSR-E SSS product), sea surface temperature analysis products and merged MERIS-MODIS colored dissolved organic matter (CDOM) absorption coefficient was estimated by interpolating the data in space and time along the path of such drifters.

As further illustrated by the example shown in Fig. 4, it takes approximately 6 months to cover a distance of 3,700 km for a freshwater particle (SSS $\sim$ 26–28) in the proximity of the Amazon mouth to relax to an open ocean surface salinity of $\sim$36. At the beginning of the period, the low SSS of water particles is modulated by mixing processes with saltier waters transported westward by the NBC rings shed at the NBC retroflection. The particle-following SSS signal modulation observed here is clearly consistent with the ocean color signal (anti-correlated with SSS), fresher water being systematically associated with colored waters showing high CDOM values, typical of the brackish plume waters. The drifter is then advected eastward along the NECC, remixed with "younger" advected plume waters in August and reached an eastern position slightly north of 8°N–38°W with an SSS of about 32 at the beginning of October. The SSS change along the drifter pathway is progressively and quasi-linearly relaxing to the open ocean values during the next 3-month period.

The link between the SSS and ocean color properties moreover enables investigations of the interactions between bio-optical and bio-chemical properties of the ocean and hydrological fluxes of terrestrial origin. Along with the freshwater, the Amazon provides the

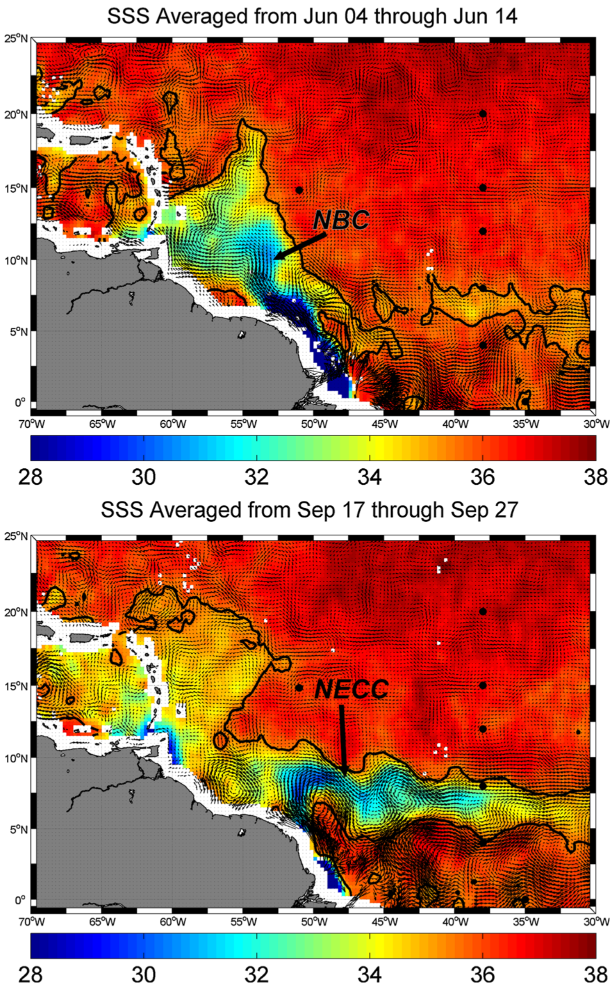

Fig. 3 Major pathways for the freshwater Amazon–Orinoco River plume detected by SMOS in 2010. Surface salinity fields from SMOS are superimposed with coinciding surface OSCAR currents estimated from altimetry and surface wind data. *Top*: the freshwater Amazon River plume is advected northwestward along the Brazilian Shelf by the North Brazilian Current (NBC) during boreal spring. *Bottom*: during boreal summer to fall period, the Amazon plume is carried eastward by the NECC. Note also the signal from the Orinoco River plume extending northeastward along the southern lesser Antilles. In both plots, the *thick black curve* is indicating the 35 SSS contour

largest riverine flux of suspended (1,200 Mt year^{-1}) and dissolved matter (287 Mt year^{-1}), which includes a dissolved organic matter (DOM) flux of 139 Mt year^{-1} (Meybeck and Ragu 1997). These fluxes can have a dramatic effect on regional ecology as they represent potential subsidies of organic carbon, nutrients, and light attenuation into an otherwise oligotrophic environment (Muller-Karger et al. 1995).

In the regions closest to the Amazon plume, light attenuation by suspended detritus acts as the main limitation to phytoplankton growth (DeMaster et al. 1996). Away from this region, as mineral detritus is removed by sinking, absorption attributable to organic

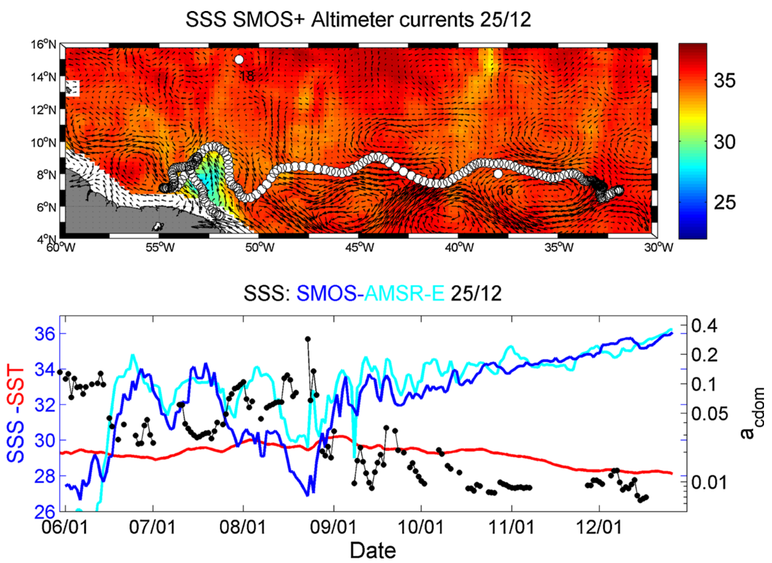

Fig. 4 *Top*: spatiotemporal evolution of the location of an hypothetical drifter (*white dots*) dropped at 52°W 6°N at the beginning of June 2010 and advected with surface currents estimated from altimetry and surface winds (*arrows*). Superimposed are the ±5 days averaged daily SSS fields from SMOS and the surface currents (*black arrows*). *Bottom*: time series of the colocalized SSS from SMOS (*blue*) and from AMSR-E (*cyan*), the analyzed SST (*red*), and the merged daily CDOM (*black*) along the drifter path

substances begins to dominate the attenuation of light in surface waters. Del Vecchio and Subramaniam (2004) studied such conditions in the Amazon plume and characterized the relative contributions of CDOM, particulate organic material, and phytoplankton to the total absorption field. In the coastal ocean adjacent to river sources, CDOM tends to behave as a freshwater tracer, decreasing away from the river source with increasing salinity. Linear correlations between CDOM and salinity in river plume waters are well documented in the ocean color literature with reported relationships robust enough to allow salinity retrievals from CDOM and vice versa (e.g., Ferrari and Dowell 1998; Palacios et al. 2009; D'Sa et al. 2002; Conmy et al. 2009).

Linearity in the CDOM–salinity relationship implies conservative mixing dominated by two distinct endmembers. Departures from linearity can occur when additional water masses are present (Blough and Del Vecchio 2002), or by in situ subsidies of CDOM released via net phytoplankton growth (Yamashita and Tanoue 2004; Twardowski and Donaghay 2001), microbial utilization (e.g., Moran et al. 1999; Obernosterer and Herndl 2000), or photochemical oxidation (e.g., Miller and Zepp 1995).

Based upon preliminary satellite microwave SSS data from AMSR-E sensor and ocean color products, Salisbury et al. (2011) recently demonstrated the spatial coherence between surface salinity and the absorption coefficient of CDOM at 443 nm in the Amazon and Orinoco river plume-influenced waters. Given the new SMOS data, the spatial and temporal coherence between SSS and optical properties of the river plumes, e.g., CDOM, can now be systematically analyzed.

As illustrated in Fig. 5, the amplitude of the annual cycle of the Amazon River discharge peaks in June–July and was apparently more important in 2010 and 2011 compared to the averaged "climatological" cycle since 1968. In comparison, the discharge from Orinoco is much lower and peaks in September. Based upon the Amazon River discharge cycle, four main periods can be distinguished as shown in Fig. 6. From November to April (low flow and ascending periods), the plume is carried northwestward with the NBC, while the summer and fall display a plume mostly carried eastward as the seasonal NECC retroflection strengthens. In comparison, the spatial pattern in the distributions of the CDOM is in general very similar to SSS during the river discharge seasonal cycle. However, the CDOM patterns can deviate from the SSS patterns at large distances from the mouth of the river for some period of the seasonal cycle. This is particularly evident in the region around the northern Antilles and the Caribbean during the high-flow season of 2010 (Fig. 6, third panel from top) whereby high CDOM values are detected north of the low-salinity plume extent (contours at SSS = 35.5 on the right panels), suggesting the presence of dissolved organic matter concentrations that are non-correlated with the Amazon River plume dilution. Altogether, this demonstrates the strength in combining satellite SSS observations with complementary satellite observations in order to better characterize the variability of the pathway of freshwater runoff along with the corresponding mixing processes at seasonal to interannual time scales.

Quasi-linear relationships between SMOS SSS and the MERIS/MODIS CDOM absorption coefficient (acdm) estimated for year 2010 are illustrated in Fig. 7. Acdm values were averaged over SSS bins with 0.5 bin width. As evidenced, while CDOM mixing processes seem to be conservative on average, clear departure from linearity is observed below 30 pss during the descending and low-flow seasons. This fact potentially indicates changes in the endmember values at the mouths of the rivers and tributaries and/or illustrate the occurrence of non-conservative mixing processes as listed above. Thanks to the new satellite observations, departure from conservative mixing and the interannual sources of variability will be certainly more detailed in the next future.

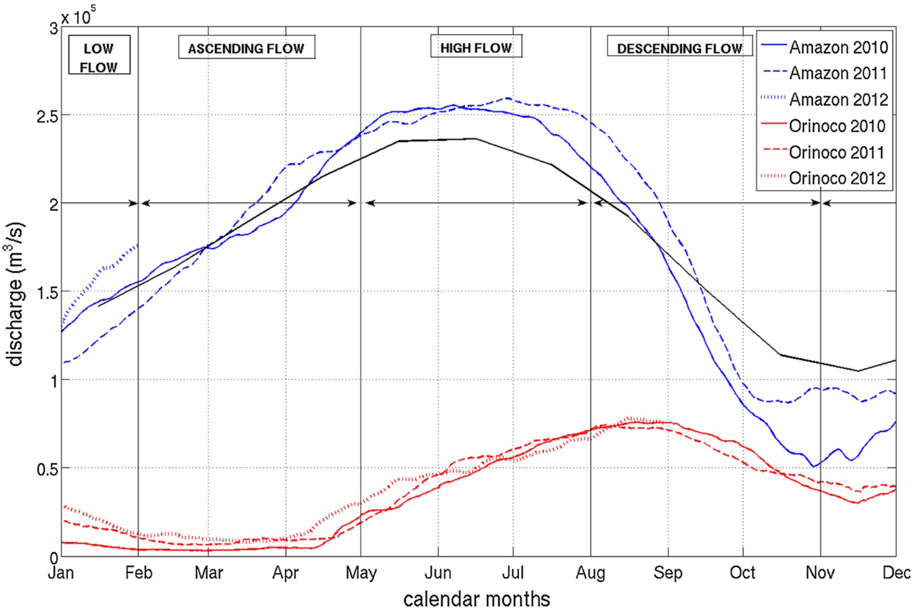

Fig. 5 Amazon (*blue*) and Orinoco (*red*) river discharge cycles measured, respectively, at Obidos and Bolivar gauges, during the period 2010–2012. The *black curve* is showing the Amazon River discharge climatology from 1968 to 2012

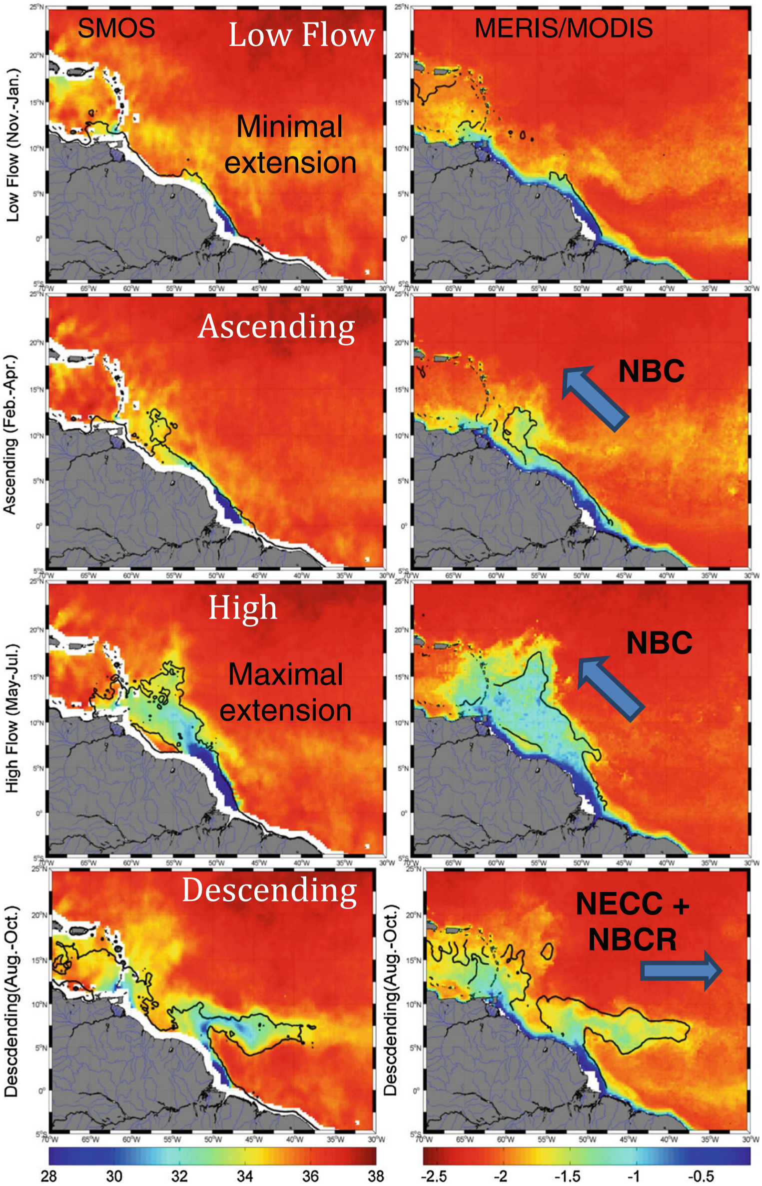

Fig. 6 Seasonal cycle of the freshwater Amazon and Orinoco river plume signals for year 2010. *Left*: SSS from SMOS averaged over the different periods of the discharge cycle. From top to bottom: low flow (November–January); ascending flow (February–April); high flow (May–July); descending flow (August–October). *Right*: corresponding CDOM absorption coefficient averaged from the merged MERIS/MODIS products. The *color bar* is logarithmic in unit of 1/m

3.2 Eastern Tropical Atlantic Freshwater Pools Monitoring

The eastern tropical Atlantic (ETA) Ocean 8°W–12°E, 6°N–20°S is a region of intense upwelling and where the second largest river in the world, the Congo, enters the ocean together with the Niger, Volta and numerous other smaller rivers (Fig. 8). In addition, intense precipitations also decrease SSS in the Guinea current and northeastern Gulf of Guinea (Hisard 1980; Merle 1980). The ETA is therefore characterized with a highly complex hydrographic system, largely influenced by the Congo River, intense precipitation, and strong seasonal coastal and equatorial upwelling in the boreal summer.

Maximum discharge from the Congo River occurs in December and minimum discharge in March through April. The outflow is hardly detectable from SST or sea level data. In chlorophyll, however, the mouth of the Congo River shows a strong signal all year round with large plumes extending offshore. While these ocean color signals highlight real oceanographic features of the plume, frequent cloud cover found in this region during the rainy season strongly inhibits the spatiotemporal evolution of the Congo plume structure to be monitored.

Hitherto the knowledge about the seasonal extension and spreading of the Congo River plume is therefore mainly relying on dedicated in situ surveys (e.g., see Meulenbergh 1968;

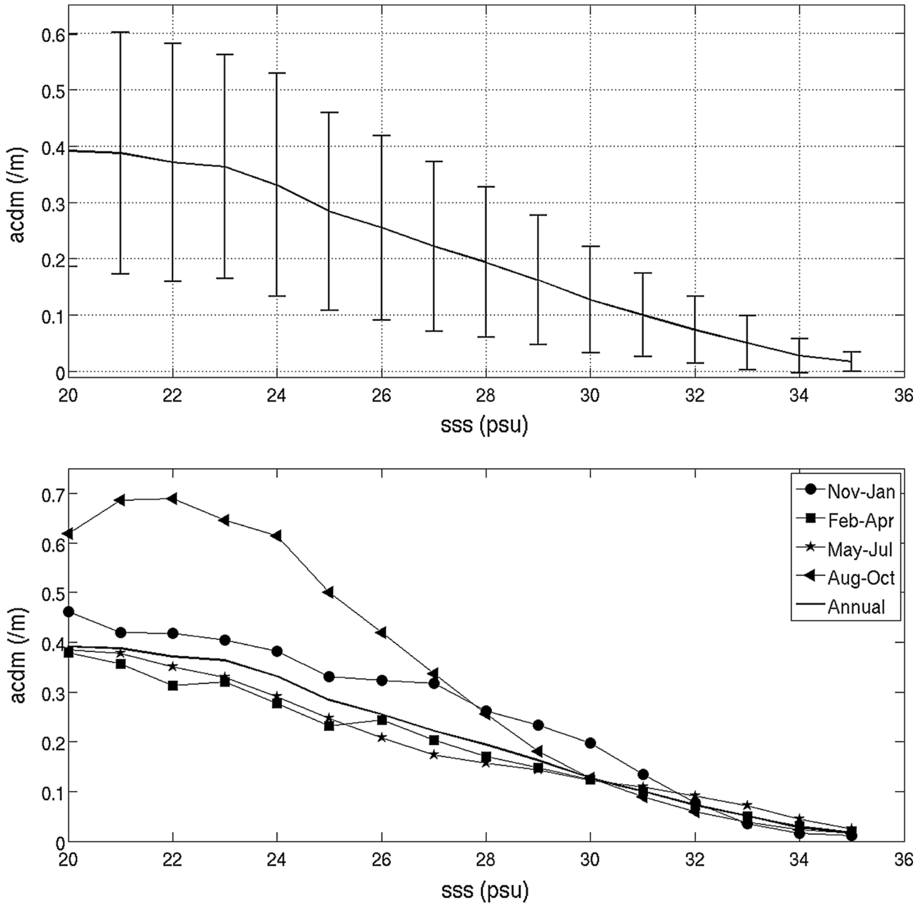

Fig. 7 $a_{CDOM}(490)$ to SMOS SSS dependence in the western tropical North Atlantic averaged over years 2010–2012 for all seasons of the Amazon River Discharge cycle (*Top*) and for each season separately (*bottom*). In the upper panel, the mean $a_{CDOM}(490)$ per 0.5 bins is shown as a *solid black line* ±1 standard deviation (*vertical bars*)

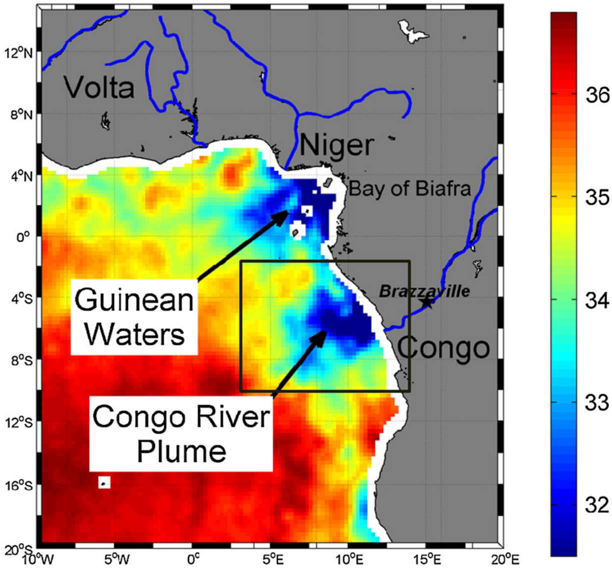

Fig. 8 Map of SMOS SSS in the Gulf of Guinea and Southeast Atlantic Ocean indicating the two largest pools of low-salinity waters in the eastern tropical Atlantic: the Bight of Biafra (Guinean waters) and the Congo River plume. The map was generated by averaging SMOS data over 2010–2012 considering only data acquired during months of April

Koleshnikov 1973;Bornhold 1973; Wauthy 1977;Van Bennekom and Jager 1978; Eisma and Van Bennekom 1978; Van Bennekom and Berger 1984; Piton and Wacongne 1985; Braga et al. 2004; Reverdin et al. 2007; Vangriesheim et al. 2009; Lefèvre 2009). However, the ensemble of in situ SSS data collected during the period 1977–2002 in the ETA is sparse, and only enabled retrievals of low-resolution ($1° \times 1°$) monthly climatology of the SSS field (Reverdin et al. 2007), as displayed in Fig. 9. Note that since 2003, the in situ SSS sampling has however improved with the increasing deployments and operations of Argo floats.

The monthly averaged SMOS SSS maps shown in Fig. 10 were generated by combining SSS data over the SMOS 3-year life period. As evidenced in detail by these maps, consistent with historical in situ observations, the Congo River plume is spreading northwestward along the coast and mixes with southwestward flowing freshwater from the bight of Biafra during February and March (Koleshnikov 1973; Wauthy 1977). In May (Van Bennekom and Jager 1978), June–July (Bornhold 1973; Wauthy 1977), and August (Koleshnikov 1973), the two fresh pools are disconnected with the Congo plume directed in westerly direction, extending up to 800–1,000 km offshore, as far as 8°E. In November, a "jet stream" of low-salinity water is ejected from the estuary with a large velocity and protrudes in WNW direction (Wauthy 1977). The plume extent can also show southward and southwestward legs depending on the prevailing windstress in the Angola Basin (Van Bennekom and Berger 1984; Dessier and Donguy 1994).

The dispersal patterns of the Congo River plume during all seasons can mostly be included inside the rectangle domain shown in Fig. 8. The 10-day running mean time series of the SMOS SSS averaged over that spatial domain is shown in Fig. 11 together with the time series of the river discharge measured at Brazaville gauge station during the period 2010–2012. Maxima in the averaged SSS within that region occur regularly in August at the time of the Congo River minimum discharge. Minima in SSS (detected

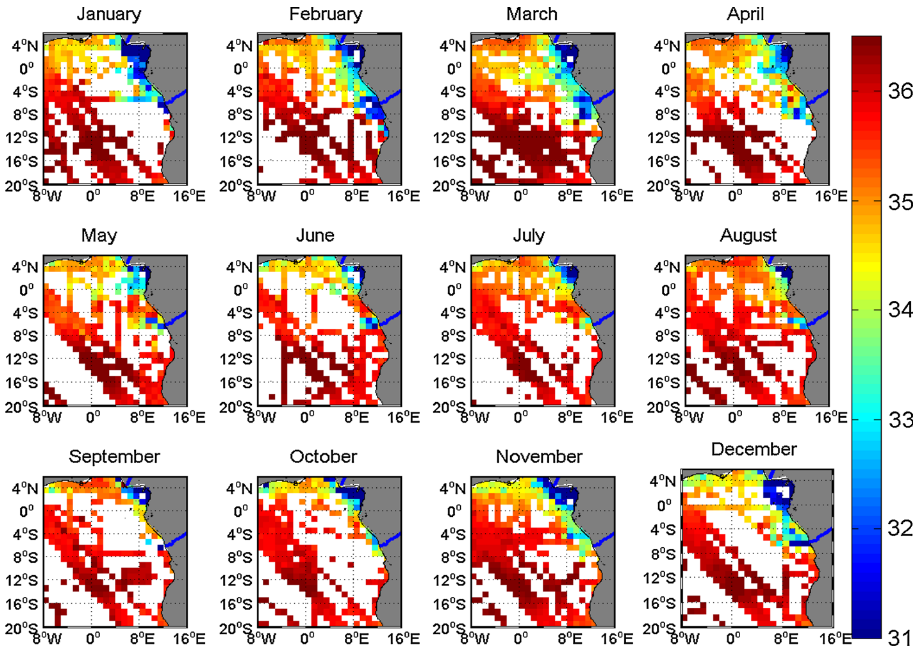

Fig. 9 Maps of the monthly averaged SSS in the ETA derived from the ensemble of in situ measurements collected during the period 1977–2002 and used to build up Reverdin et al. (2007) climatology

around April), however, lag by approximately 4 months the maxima in the river discharge at Brazaville station (found around December–January). These lags probably indicate the time for the freshwater masses to be transported from Brazaville to the river mouth and then to be further advected by surface currents far offshore. However, the interannual variability in the amplitude of the seasonal cycle of SSS and river discharge are not correlated. While the river discharge reached significantly different minimum values of $\sim 3.3 \times 10^4 m^3/s$ and $\sim 2.3 \times 10^4 m^3/s$ in 2010 and 2011, respectively, the maxima in the averaged SSS are constantly found at $\sim$35.5 pss. Similarly, the maximum discharge level of $\sim 5.8 \times 10^4 m^3/s$ measured over the period is found in January 2012, while the minimum in the averaged SSS ($\sim$31.9) occurred in April 2011.

While understanding the observed satellite SSS trend in that region is still an undergoing activity, combining satellite information on surface currents, SST, rain rates and SSS together with river discharge levels will certainly help in the near future to better quantify the sources of variability in the local hydrological cycle of the Gulf of Guinea. The terrestrial and atmospheric hydrological fluxes in this region also act as a dominant modulator of the local fishery. The regular SMOS SSS data can therefore help to better understand the mechanisms involved in the biophysical interplay and its relevance for the fishery with potentially significant socioeconomic impact in that region.

In addition, similarly to the Amazon–Orinoco River plumes, conservative mixing laws for bio-optical properties of the major river plume in the ETA region can now be systematically studied using SMOS data as shown in Fig. 12. Examples of the conservative mixing linear laws for the CDOM coefficient deduced only from space-borne measurements are shown for year 2010 around the Congo and Niger rivers.

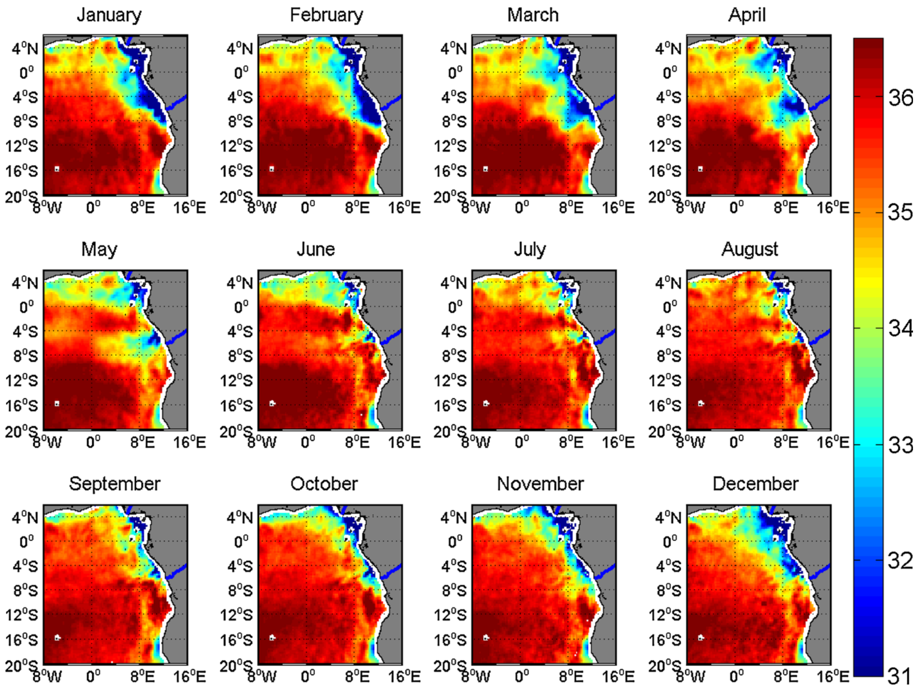

Fig. 10 2010–2012 Monthly averaged seasonal cycle of surface salinity in the eastern tropical Atlantic derived from SMOS observations

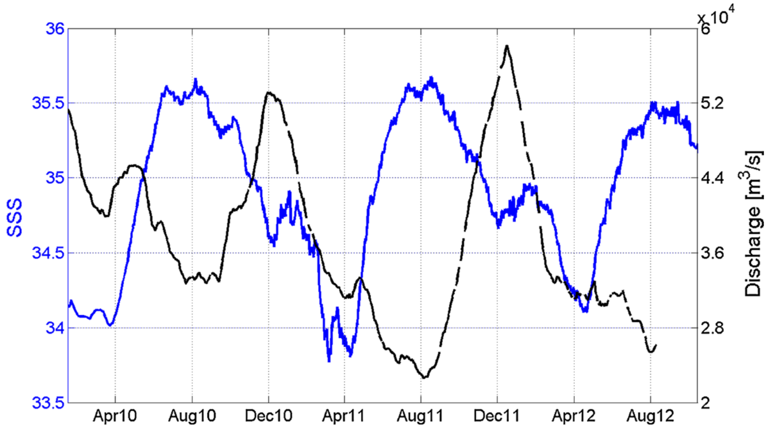

Fig. 11 Times series of (i) the SMOS SSS averaged over the spatial domain (3°–14°E;10°–2°S) illustrated by the *black rectangle* in Fig. 8 (*blue*) and (ii) of the Congo discharge level measured at Brazaville (*black*)

4 Precipitation Signatures in SSS Data from Space

Large vertical gradients can develop in the upper few meters of the ocean after a heavy rainfall, as first evidenced during the Tropical Oceans-Global Atmosphere Coupled Ocean–Atmosphere Response Experiment (TOGA COARE) (Soloviev and Lukas 1996;

Schlössel et al. 1997; Wijesekera et al. 1999). The downward freshwater flux at the sea surface establishes a haline diffusive molecular layer (or freshwater skin of the ocean) (Katsaros and Buettner 1969) that is characterized by a salinity gradient, with salinity differences across this freshwater skin sometimes greater than 4 salinity units. The residual effects of the rain-induced skin layers can even be stronger at the highest rain rates (Schlössel et al. 1997). This freshwater skin stabilizes the near-surface layer (Ostapoff et al. 1973) and tends to dampen free convection in the upper oceanic boundary layer.

These conditions motivate the development of autonomous SSS drifters able to monitor the salinity at less than 50-cm depth. Using such instruments, Reverdin et al. (2012) documented salinity freshening between 15-cm and 50-cm depth in the tropical oceans. Sudden salinity decreases are often associated with local rainfall and vertical salinity gradients that last for a few hours, depending, among other factors, on wind speed conditions. The haline molecular diffusion layer that is established in the upper ocean during rainfall can thus be important for the radiometric observation of the sea surface at low microwave frequencies. At centimeter wavelengths, the dielectric constant is modified by the sea surface salinity (e.g., Klein and Swift 1977; Yueh et al. 2001) and any change of the latter might cause interpretation problems when comparing remotely measured surface salinity at these frequencies to deeper in situ measurements.

Hence, under rainy conditions (or just after a rainfall), the satellite-derived SSS better characterizes the salinity at the ocean–atmosphere interface rather than the 1–10-m deep in situ samples. Whether accumulated precipitation can be estimated from changes in salinity at the ocean surface as observed from space remains, however, an open question, as assumptions have to be made about the penetration depth of the freshwater. In addition, assimilation of the new satellite SSS data into ocean circulation models having limited vertical resolution also challenges our modeling perspectives concerning the dynamics of the first centimeters to first meter of the ocean surface.

In the following section, we discuss signatures of precipitation detected in the new SMOS SSS data. First, the strong SSS spatiotemporal variability associated with rain

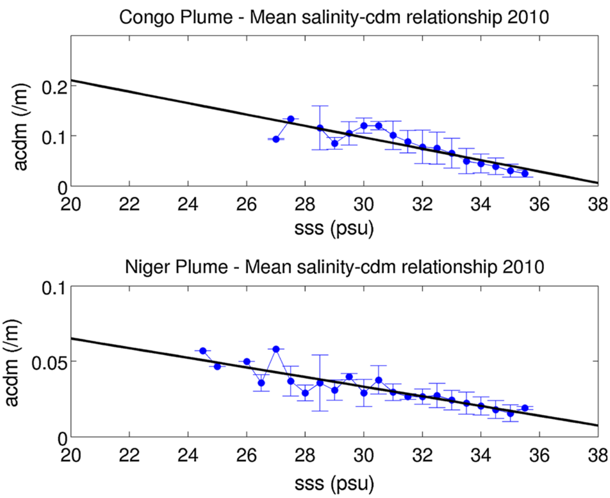

Fig. 12 $a_{CDOM}(490)$ to SMOS SSS dependence in the eastern tropical Atlantic averaged over year 2010 for the Congo(*Top*) and Niger (*Bottom*) River Plumes. The mean $a_{CDOM}(490)$ per 0.5 bins is shown as a *solid black line* ±1 standard deviation (*vertical bars*)

events as seen both by space-borne and in situ sensors in the Pacific Ocean Inter Tropical Convergence Zone is presented. Second, it is revealed that the SSS from space is systematically showing lower values (negative bias) with respect to the deeper 5–10 m depth of Argo upper salinity in this area. These effects are shown to be statistically correlated with rain. Third, long-lived, large-area, and large-amplitude SMOS SSS anomaly patterns in the tropical Atlantic are shown to follow local anomaly patterns in the evaporation–precipitation (E–P) budget. Finally, some preliminary results concerning the interannual variability of the SMOS SSS signal in the Indian and in the tropical Pacific oceans and connections to key climate indexes will be presented and discussed.

4.1 SSS Temporal Variability Associated with Rain Events

Although satellite observations provide a better sampling of the global ocean than the in situ observing systems, such as the Argo float array, individual SSS measurements are obtained in rainy regions with a strong temporal variability seen on both SMOS and Argo SSS. In Fig. 13, we show such an example of colocated SMOS and Argo profiler measurements in the Inter Tropical Convergence Zone of the Tropical Pacific, indicating a significant surface freshening associated with a rain event. On August 11, 2010, the Argo float WMO id#4900325 detected a freshening of 0.9 between 20- and 5.5-m depth (Fig. 13a). In contrast, the Argo profile derived on 22 August shows that the salinity between 30- and 5-m depth is much more homogeneous with more saline water at 5-m depth compared to the one recorded on 11 August.

The TRMM satellite rain rate (RR) estimates averaged over a $2° \times 2°$ box centered on the Argo float location indicate a significant rain rate of 1–2 mm h^{-1}on 11 August that lasted for at least a day before the Argo profile raised to the surface (Fig. 13c). Contrarily, negligible precipitation occurred on 22 August and during the preceding week. The first SMOS pass collocated with the 11 August Argo profile (Fig. 13a) was acquired also during rainy conditions and showed a low SSS of $\sim$32.8 (0.1 saltier than the Argo SSS taken 6:30 h later, Fig. 13c). The second SMOS pass on the 16 August occurred under non-rainy condition (Fig. 13c) and is 0.5 saltier. Consistent with the 22 August Argo profile (Fig. 13b) observations, the collocated SMOS SSS during these rain-free conditions (Fig. 13c) are also significantly saltier by 0.4–0.6. The large SSS variation (0.7) measured by this Argo float at a 10-day interval and by the collocated SMOS measurements over several SMOS passes clearly demonstrates the influence of the rain timing on the SMOS-Argo SSS differences.

4.2 Systematically Fresher Skin SSS in Rainy Regions

The SMOS SSS map averaged over July–September 2010 is compared to optimally interpolated in situ ISAS map averaged over the same period shown in Fig. 14. At large scale, SSS spatial variability sensed by SMOS is consistent with ISAS. A striking visual feature of the SMOS SSS map compared to the ISAS map in the tropics is the freshest SSS in the North Tropical Pacific, under the location of the ITCZ (particularly west of 120°W).

When SMOS SSS are precisely colocated around Argo SSS in various regions of the global ocean (see Boutin et al. 2012a, b), a more negative bias (~ -0.1 than in other regions) and larger standard deviation are systematically observed between 5° and 15°N in the Pacific Ocean with respect to other regions (Table 2).

To investigate whether a systematic negative bias of $\sim$0.1 between the satellite skin depth SSS and the $\sim$5-m depth Argo floats data could be related to rain-induced vertical

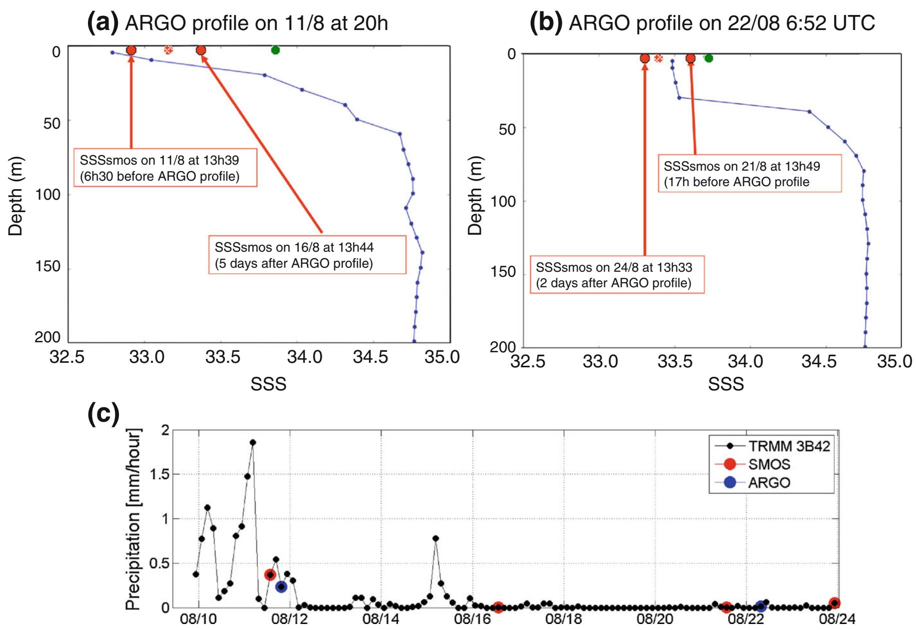

Fig. 13 Two successive Argo profiles taken by float 4900325 (*blue curve*) in the eastern tropical Pacific on **a** 11 August 20:00 UTC (latitude = 12.4°N; longitude = 117.6°W) and **b** 22 August 6:52 UTC (latitude: 12.2°N; longitude: 117.8°W). Mean SMOS SSS collocated within a 5-day window and a radii of 50 km with these profiles are indicated by red dashed point. In each case, two SMOS passes have participated to these collocations: mean SMOS SSS corresponding to each pass is indicated as red filled point. The corresponding ISAS SSS in August is indicated by the green point. The time series of the 3-hourly satellite rain rate from TRMM 3B42 and averaged over (11°–13°N; 116°–118°W) is provided in (**c**). The time at which SMOS and Argo acquired SSS data is indicated by red and *blue dots*, respectively

stratification, a triple collocation between Argo, SMOS level 2 products (at ~40-km resolution, non-averaged in time) and SSMI satellite rain rate (RR) data was conducted. SMOS and SSMI RR data were colocated within a temporal window of −40 min and +80 min, while a ±5-day windows was considered to colocate SMOS and Argo data.

The theoretical error on the SMOS SSS retrieved level 2 data used in this colocation exercise is ~0.5. Without any RR sorting, the statistical distribution of the differences *ΔSSS* is skewed toward negative values (Fig. 15, Table 3); when only SMOS non-rainy events are considered, the negative skewness disappears, and statistics of the SMOS–Argo differences in the tropical Pacific Ocean become close to the ones in the subtropical Atlantic Ocean (Tables 2, 3). Largest skewness toward negatives differences is obtained when only SMOS SSS close to rain events are considered. For these rainy SMOS cases, we find a negative dependency of the SMOS–Argo SSS differences with respect to SSMIs RR of −0.17 pss/mm^{-1} h, i.e., a freshening of 1.7 for a SSM/I RR of 10 mm h^{-1}(Boutin et al. 2012a, b).

The non-sorting of SMOS measurements close in time with rain events in SMOS–Argo collocated data sets (within 10 days and 100 km) is responsible for (1) a mean −0.1 negative bias over 3 months between 5° and 15°N in the tropical Pacific region with respect to non-rainy conditions and with respect to the subtropical Atlantic region and (2) a negative skewness of the statistical distribution of SMOS minus Argo SSS difference (Fig. 15). Given that the whole set of SMOS–Argo collocations also includes the situations with rainy Argo measurements collocated with non-rainy SMOS measurements, these results indicate a

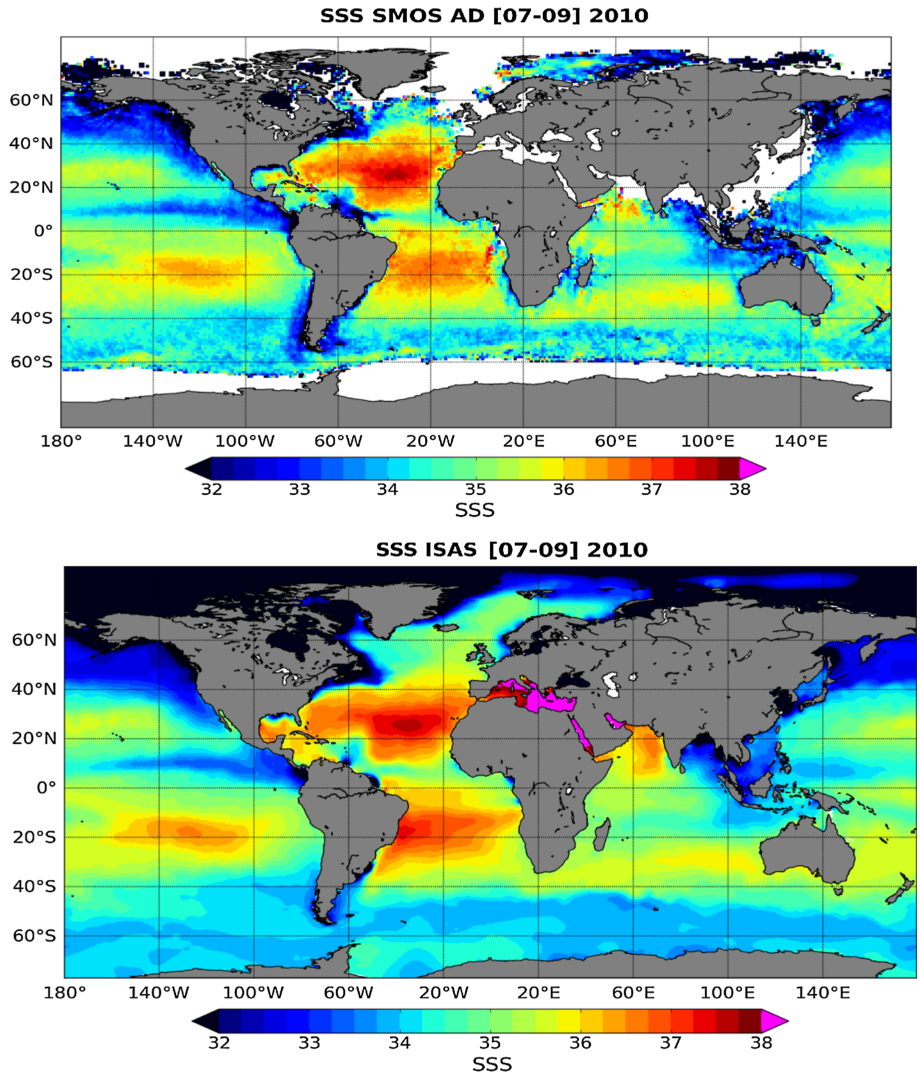

Fig. 14 Maps of SSS averaged from July to September 2010, derived from (*top*) SMOS ascending and descending orbits and ISAS (*bottom*)

systematic freshening of SMOS SSS in rainy conditions and are likely a signature of the vertical salinity stratification between the first centimeter of the sea surface layer sampled by SMOS and the 5-m depth sampled by Argo. For more detail on the vertical SSS stratification induced by rain, the reader is also referred to Boutin et al. (2012b).

4.3 SSS as a Tracer of the Evaporation–Precipitation Budget in the Oceanic Mixed Layer

The SMOS-derived SSS can also be used to investigate the consistency between observed SSS variability and the evaporation minus precipitation budget in the ITCZ of the tropical

Table 2 Comparison of SMOS SSS (10 day, 100 × 100 km^2 average) values, in pss, collocated with a total of N Argo upper depth measurements

	Mean (ΔSSS)	Std (ΔSSS)	*N*
Subtropical Atlantic Ocean (15°–30°N; 45°–30°W)	−0.13	0.28	206
Tropical Pacific Ocean (5°–15°N; 180°–110°W)	−0.23	0.35	692
Southern Indian Ocean (40°–30°S; 70°–90°E)	0.04	0.39	114
Southern Pacific Ocean (50°–40°S; 180°–100°W)	−0.08	0.51	467

$\Delta SSS = SSS_{smos} - SSS_{argo}$ Only SMOS ascending orbits are considered. Std (ΔSSS) primarily reflects the decreasing signal to noise ratio with decreasing SST. Note that subtropical Atlantic Ocean and tropical Pacific Ocean have similar SST

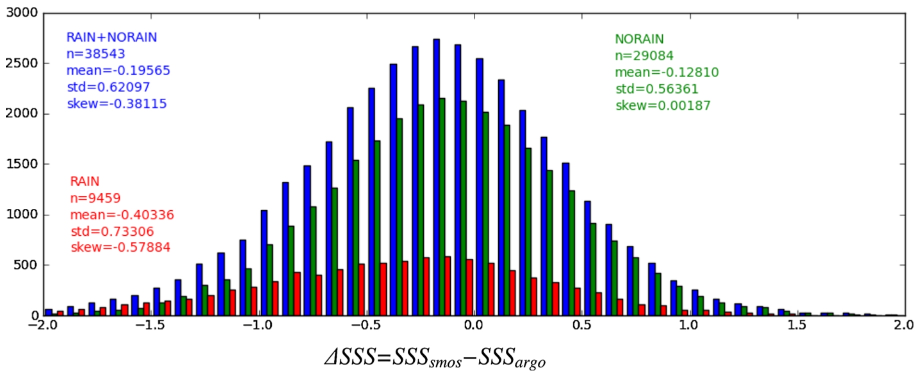

Fig. 15 Statistical distribution of SSS differences $\Delta SSS = SSS_{smos} - SSS_{argo}$ in the tropical Pacific Ocean for various sorting on colocated SSSM/I rain rates. *Blue*: all collocations (without any rain sorting); *green*: for non-rainy cases (SSM/I rain rates less than 0.1 mm h^{-1}); *red*: rainy cases (SSM/I rain rates larger than 0.1 mm h^{-1}). Corresponding statistics are indicated in Table 3

Table 3 Statistics for the SSS differences $\Delta SSS = SSS_{smos} - SSS_{argo}$as a function of rain rate (RR) in the northern tropical Pacific Ocean

	Mean (ΔSSS)	Std (ΔSSS)	Skew (ΔSSS)	*N* (ΔSSS)
Tropical Pacific (5°–15°N; 110°–180°W)				
All colocations	−0.20	0.62	−0.38	38,543
No rain (RR < 0.1 mm h^{-1})	−0.13	0.56	0.01	29,084
Rainy (RR ≥ 0.1 mm h^{-1})	−0.40	0.73	−0.58	9,459

Atlantic based upon the SSS and SST relationship in the ocean mixed layer (OML). The salt conservation budget in the OML with depth h can be expressed as follows (Michel et al. 2007; Yu 2010, 2011):

$$\frac{\partial S}{\partial t} = \frac{(E - P - R)S}{h} - \vec{u} \cdot \nabla S - \Gamma(w_e)\frac{w_e(S - S_h)}{h} + k\nabla^2 S \quad (1)$$

where S is the surface salinity, t is time, E and P the evaporation and precipitation rates, respectively, R the freshwater input by river runoffs, h the mixed layer depth, $\vec{u}$ the (vertically averaged) current vector within the OML, and w_e the vertical entrainment rate.

S_h is the salinity just below the OML, k is the horizontal diffusivity coefficient ($k \sim 2{,}000\ \mathrm{ms}^{-2}$). The total entrainment term must be treated differently in case of upward or downward entrainment, so it is multiplied by a step function Γ in Eq. (1). Indeed, when additional water is included into the mixed layer, its properties are affected by mixing with the deeper layer: $\Gamma(w_e) = w_e$ if $w_e > 0$. On the contrary, if water is removed from the mixed layer, the properties of the remaining water are conserved and only its depth h can change: $\Gamma(w_e) = 0$ if $w_e < 0$. The vertical processes are conveniently represented by a single entrainment term, consisting of the vertical Ekman advection and the OML conditions.

The first term in the right-hand side of Eq. (1) is the net freshwater flux. The impact of this flux on the surface water strongly depends on the salinity itself. Moreover, SSS has no direct feedback on the surface flux. These particularities have important consequences on the salt budget and on the duration of SSS anomalies. The second term is the horizontal advection of salinity by surface currents that can be separated into a wind-induced component, the Ekman transport, and the geostrophic current. Ekman transport is due to wind friction on the sea surface, which is rotated by the Coriolis force as it penetrates in depth. The Ekman layer depth is systematically lower than the mixed layer depth, because both increases with the wind stress, although the depth of the mixed layer also deepens in response to other processes. Thus, the Ekman transport occurs entirely in the OML. In addition, the geostrophic current that arises from the balance between the horizontal pressure force and the Coriolis force can usually be considered constant, with the mixed layer resulting from the homogeneous density structure.

The value of the SMOS SSS at a fixed point, $S(t, r)$, is obtained by averaging individual SMOS swath SSS measurements over a considerable time interval ($t - \tau/2$, $t + \tau/2$), say 10 days, which is enough to filter out noise in the SSS. Suppose that the climate mean, or norm, of this SSS (provided by climatology) is $\overline{S(t,r)} = S_o(t,r)$. In the following, we define the SSS anomaly as the departure of the SSS from the norm:

$$\Delta S(t,r) = S(t,r) - S_o(t,r)$$

Following approaches traditionally used for studying large-area SST anomalies (Piterbarg, and Ostrovskii 1997), a formal definition can be introduced for the large-area SSS anomalies. For example, large-area and large-amplitude SSS anomaly comprises the connected components of the set:

$$\{(x,y) : |\Delta S(t,r)| > S_T\}$$

where $r = (x, y)$ and S_T is a threshold that can be taken either as a fixed salinity value, for example, 0.2 pss or as a function of the standard deviation of SSS anomalies, σ_S, for example, 0.5 σ_S. This choice for the threshold depends on the magnitude of the anomaly of interest.

In the tropical Atlantic, Michel et al. (2007) and Yu (2011) have shown that the dominant terms of the mixed layer salinity balance are horizontal advection by Ekman and geostrophic currents and the atmospheric forcing fluxes ($E - P - R$). In that context, the salinity balance equation in the OML can be simplified as follows:

$$\frac{\partial S}{\partial t} \cong \frac{(E-P-R)S}{h} - \vec{u} \cdot \nabla S \qquad (2)$$

Using OSCAR surface current products (which comprise contributions of both Ekman and geostrophic currents), the horizontal salt advection term $\vec{u} \cdot \nabla S$ can be deduced from

SMOS observations. The following residual SSS anomaly can then be estimated from SMOS temporal observations of salinity $S(t, r)$ at point r following:

$$\Delta S(t,r) = S(t,r) - S_o(t,r) - \vec{u}(t,r) \cdot \nabla S(t,r) \tag{3}$$

According to the simplified salinity balance (Eq. 2), a priori valid for the tropical Atlantic, the resulting SSS anomaly given by Eq. 3 shall be strongly correlated with the net freshwater flux forcing term. Examples for such SSS anomaly analysis are shown in Fig. 16 for a selected point in the middle of the north tropical Atlantic (16°N–35°W). From TRMM precipitation and OAFLUX daily evaporation fluxes, large-area P and E anomalies were also evaluated:

$$\Delta P(t,r) = P(t,r) - P_o(t,r)$$
$$\Delta E(t,r) = E(t,r) - E_o(t,r)$$

where P_o and E_o are the local climate mean for the precipitation and evaporation.

As illustrated in Fig. 16 (middle right panel), very significant long-lived negative $\Delta S(t, r)$ values are detected in SMOS anomalies at the selected point in the north tropical Atlantic during September/October months (days 250–300) of 2010. Apparently, this happened just after a strong positive anomaly in the precipitation rate as detected from TRMM during the passage of the ITCZ in August (bottom right panel).

The spatiotemporal consistency between the large-area and large-amplitude S, P and E anomalies can be further analyzed over all the tropical Atlantic. This is illustrated in Fig. 17 for two selected months of 2010. The spatial distribution of the large-area and long-lived (monthly averaged) SSS anomalies generally matches well the spatial patterns for the large E–P anomalies. In particular, north–south oscillation in $\Delta S(t, r)$ around the ITCZ (centered on 5°N in March and 8°N in July) follows the ΔE–$\Delta P(t, r)$ far from the Amazon plume area, with negative $\Delta S(r, t)$ corresponding to positive $\Delta P(t, r)$ and positive $\Delta S(r, t)$ found in region of positive $\Delta E(t, r)$. The average relationship between SMOS SSS anomalies and the corresponding anomalies in the net atmospheric freshwater flux in the tropical Atlantic (defined here by 5°S–20°N;75°W–15°E) was further evaluated over year 2010 by binning $\Delta S(t, r)$ values as function of ΔE–$\Delta P(t, r)$ as shown in Fig. 18.

Despite a significant scatter in the data, the results clearly indicate the strong coherency between SMOS SSS anomalies and the evaporation minus precipitation flux signal in the tropical Atlantic. On average, SMOS SSS are thus systematically fresher than the SSS climatology when precipitation rate exceed evaporation rate with respect climatological means, and vice versa. As expected by the skin layer effects (Zhang and Zhang 2012), satellite SSS anomalies are weakly sensitive to excess evaporation showing an almost constant value whatever positive values for ΔE-ΔP. Nevertheless, and as discussed in Sect. 4, the average 0.3 salinity unit excess amplitude found for ΔS in evaporative zones is significantly larger than the expected evaporation-induced effect on the satellite $\sim$0.01 pss. The source for such observed signal amplitude is not yet understood. Other physical processes, not yet well accounted for in the SSS retrieval algorithm, may systematically affect the L-band brightness temperature in strongly evaporative zone (e.g., skin effects in SST, badly accounted for roughness effects at low winds).

Nevertheless, Fig. 18 clearly shows that SSS anomalies become increasingly negative as the precipitation anomalies progressively exceed the evaporation anomalies.

This shows that it is important to monitor SSS from space in the rainy regions as it makes a good oceanic rain gauge for the changing water cycle (Cravatte et al. 2009; Yu 2011; Terray et al. 2011), and therefore help to maintain a continuous observation network

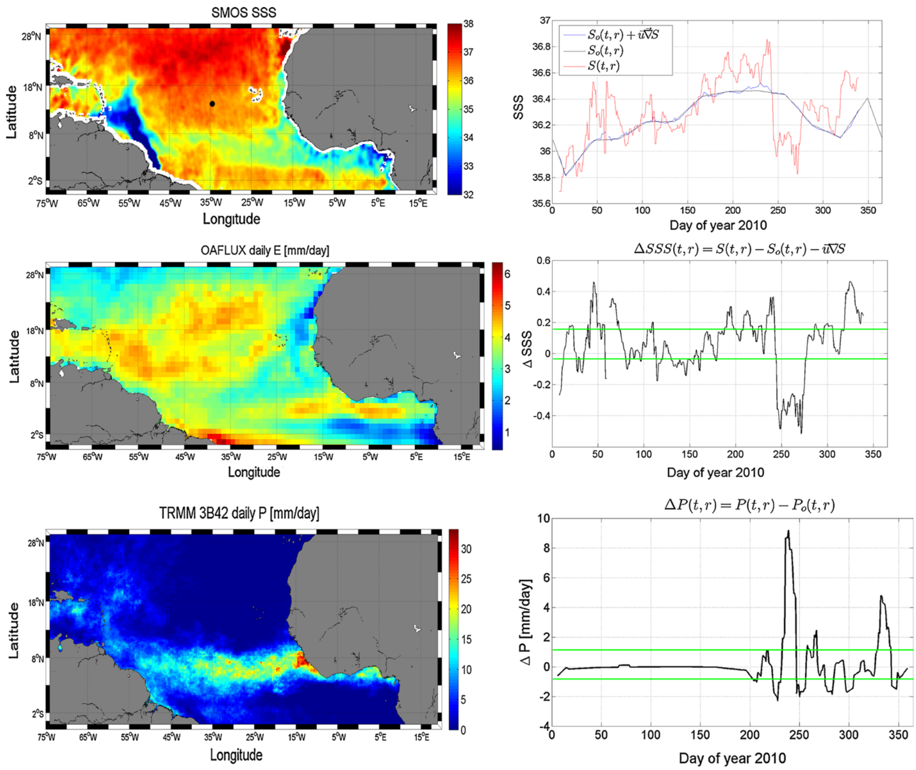

Fig. 16 *Top left*: SMOS 10-day SSS field in June 2010. *Top right*: time series of the surface salinity S(t) at the *black point* shown in the top left figure (35°W; 16°N). *Red*: SMOS SSS, *blue curve*: local mean climatological annual cycle at that point $S_o(t)$. The resulting time series for the SMOS anomaly ΔSSS at that point is shown in the middle panel, right plot. The *green horizontal lines* are indicating ± one standard deviation of the local SSS anomalies, σ_S. In the *middle* and *bottom left panels*, we show the corresponding OAFlux evaporation and TRMM 3B42 precipitation field (mm/day). The time series of the precipitation anomaly at the point is shown in the *bottom right panel*

in these key regions of the marine branch of the global hydrological cycle. In that context, SMOS SSS may therefore be an interesting data set for assimilation into ocean models in the perspective of better constraining oceanic precipitation forcing terms.

4.4 Large-scale SSS Interannual Variability in Tropical Indian and Pacific Oceans

In the Indian and Pacific oceans, the precipitation impact on the large-scale SSS variability can also be observed from SMOS and ISAS monthly maps.

The 2010–2011 period was characterized by a strong La Niña event lasting from July 2010 to March 2011 and by an Indian Ocean Dipole (IOD) index in negative phase in September–November 2010 and in positive phase during about the same months in 2011 (see Fig. 19). Such events are known to generate large-scale SSS signatures in the tropics (e.g., Gouriou and Delcroix 2002; Singh et al. 2011; Grunseich et al. 2011) and are clearly depicted in the SSS signals in both the ISAS and the SMOS monthly difference maps between 2010 and 2011 for both July and November (Fig. 20).

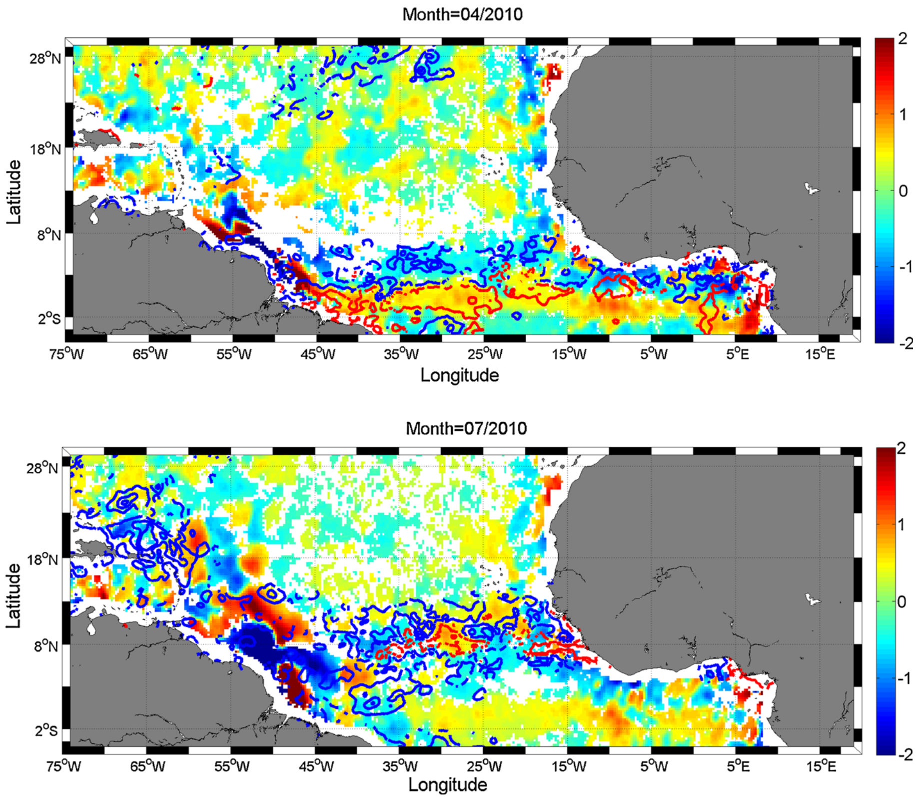

Fig. 17 Maps of the monthly averaged large-amplitude SSS anomalies deduced from SMOS data for 2 selected months of 2010 (*Top*: month of March 2010. *Bottom*: month of July 2010). The threshold value used to derive the anomaly is defined by 1 σ_S, the local standard deviation of SMOS anomaly. Superimposed are the contours of the large positive amplitude precipitation anomalies (*blue*) and positive evaporation anomalies (*red*)

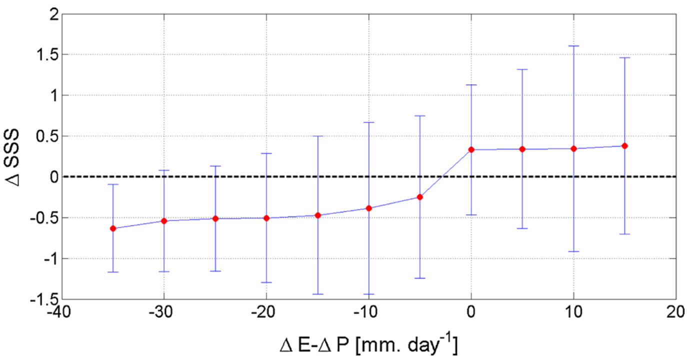

Fig. 18 Average relationship between SMOS SSS anomalies and the net atmospheric freshwater flux anomalies ΔE–ΔP in the tropical Atlantic (defined here by 5°S–20°N;75°W–15°E) over year 2010

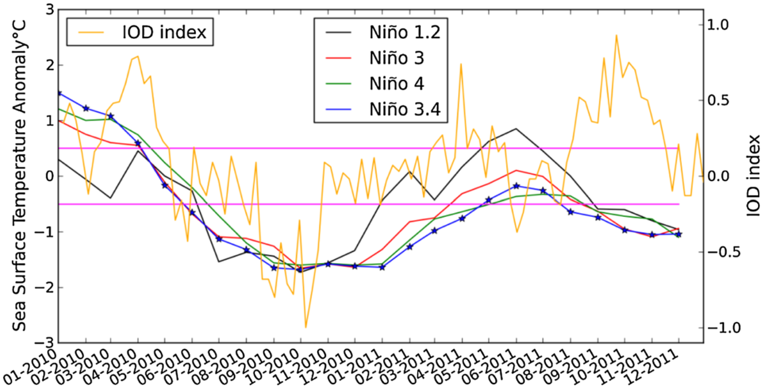

Fig. 19 Time series of SST anomalies in the four Niño regions from http://www.cpc.ncep.noaa.gov/data/indices/sstoi.indices in 2010–2011 and corresponding Indian Ocean Dipole (IOD) Index (SST difference between eastern and western equatorial Indian Ocean) from the Australian bureau of Meteorology (BOM)

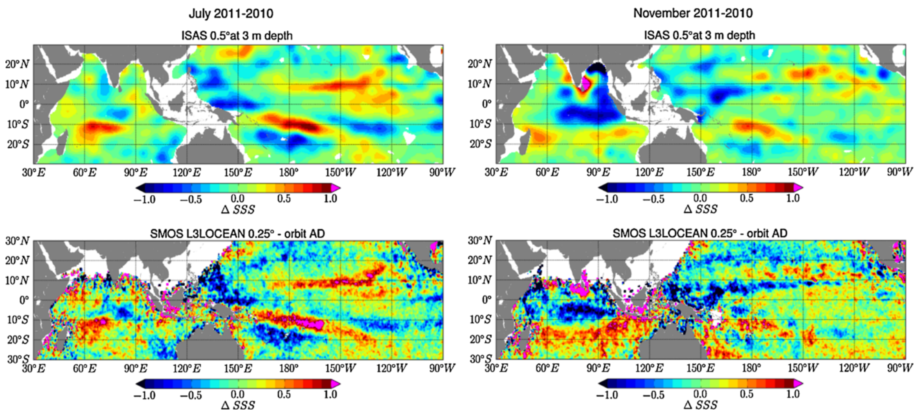

Fig. 20 Differences in the monthly averaged SSS between year 2011 and 2010 for months of July (*left*) and November (*right*). *Top panels* show the $\Delta SSS = SSS_{2011} - SSS_{2010}$ results obtained from in situ OI analysis products ISAS and bottom ones from SMOS data

The differences in rain rate as derived from SSM/I F17 sensor between 2011 and 2010 for several selected months as shown in Fig. 21 further demonstrate that part of the observed SSS interannual variability for July and November is associated with large precipitations anomalies during previous months, associated with displacements of the ITCZ and of the South Pacific Convergence Zone. In the Indian Ocean, SSS differences $\Delta SSS = SSS_{2011} - SSS_{2010}$ observed in November indicate saltier SSS in 2010 than in 2011 in the eastern equatorial Indian Ocean within the band [10°–0°S; 70°–95°E] associated with a smaller rain rate ($RR_{2010} < RR_{2011}$) in the surrounding region during preceding months, as evidenced by the rain rate difference on the October and November maps shown in Fig. 21. Between ~10°S and 20°S, SSS are fresher in 2010 than in 2011; this is associated with higher precipitation in 2010 than in 2011($RR_{2011} < RR_{2010}$) in the eastern basin but not over the whole basin. Patterns of positive SSS anomalies in the eastern equatorial Indian Ocean and negative anomalies in the eastern part of the region south of ~10°S are quite consistent with SSS anomalies already reported during negative IOD coupled with a strong La Niña event (see Fig. 8 of Grunseich et al. 2011).

Although patterns of 2011–2010 SSS differences are similar on SMOS and ISAS monthly maps, the differences are often more contrasted in the SMOS data (e.g., Fig. 20, left part and Fig. 22).

This originates from fresher SSS seen in the SMOS SSS maps than in the ISAS SSS maps (Fig. 22). In addition, the spatial extent of the low SSS region appears wider in the SMOS map, as illustrated in Fig. 22 left, around 8°N. This is possibly due to the in situ

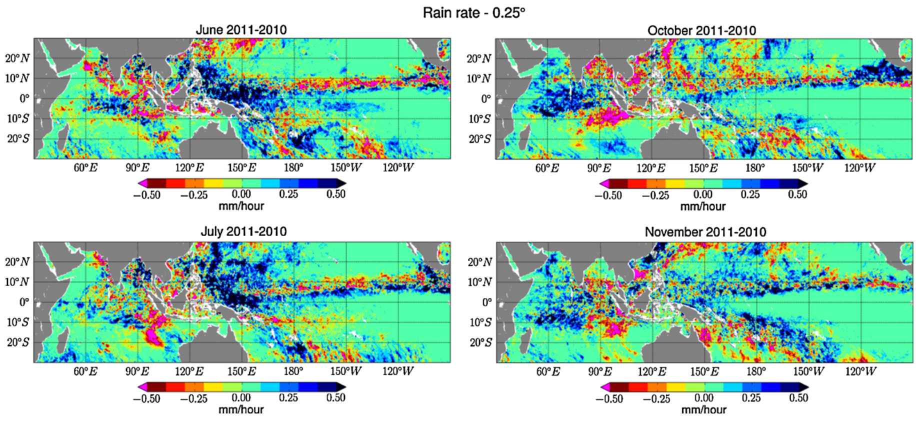

Fig. 21 Rain rate differences $\Delta RR = RR_{2011} - RR_{2010}$ derived from SSM/I F17 between 2011 and 2010 for months of June (*top left*); July (*bottom left*), October (*top right*), and November (*bottom right*)

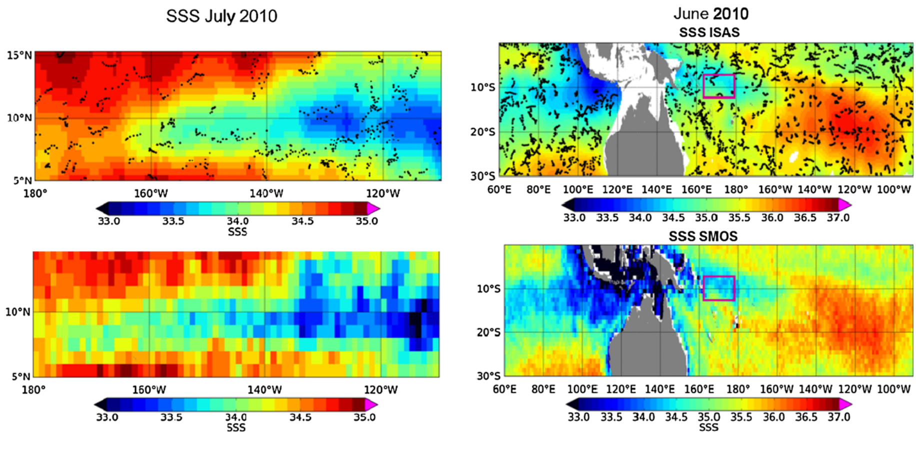

Fig. 22 *Left*: July 2010 SSS maps in the northern tropical Pacific Ocean from ISAS (*top*) and SMOS (*bottom*). *Right*: June 2010 SSS maps in south Pacific–Indian tropics from ISAS (*top*) and SMOS (*bottom*). In both top panels, the *small black dots* represent the locations of the in situ data samples used in the objective analysis. The *purple square* on the *right figure* indicates the region where the drifter discusses in Fig. 23 evolved

measurements undersampling and/or smoothing by the OI applied to the ISAS. In addition, the SMOS freshening could be linked to the different depth of the measurements (SMOS at 1 cm and in situ SSS measured at several meters depths) as described in Sects. 4.1 and 4.2.

Finally, to illustrate the potential impact of the vertical stratification effect on the ΔSSS differences between satellite and in situ, we compare along the drifter trajectory the salinity measured at 45-cm depth by a surface float (Reverdin et al. 2012) in the 2010 rainy western Pacific with monthly SSS maps (Fig. 23). The drifter SSS data clearly indicate a large signature of rainy events, with typical freshening events 1 pss for more than 1 day. The ISAS SSS is on the upper range of the drifter SSS, while monthly SMOS SSS is systematically on the lower range in this rainy region. While more work is certainly needed to determine the physical sources for these observed differences, the vertical SSS stratification associated with rain events, as illustrated by this case, is a likely contributor to the different signatures in the interannual SSS variability as detected by the SMOS satellite SSS data and the Argo data.

These preliminary results confirms the capability of L-band radiometry in detecting large SSS signals and their low-frequency variability (here over a 2-year period), in spite of much noisier satellite than in situ measurements. In general, this results from much better satellite-based temporal coverage and with a better spatial resolution, thus offering complementary information to existing in situ measurements.

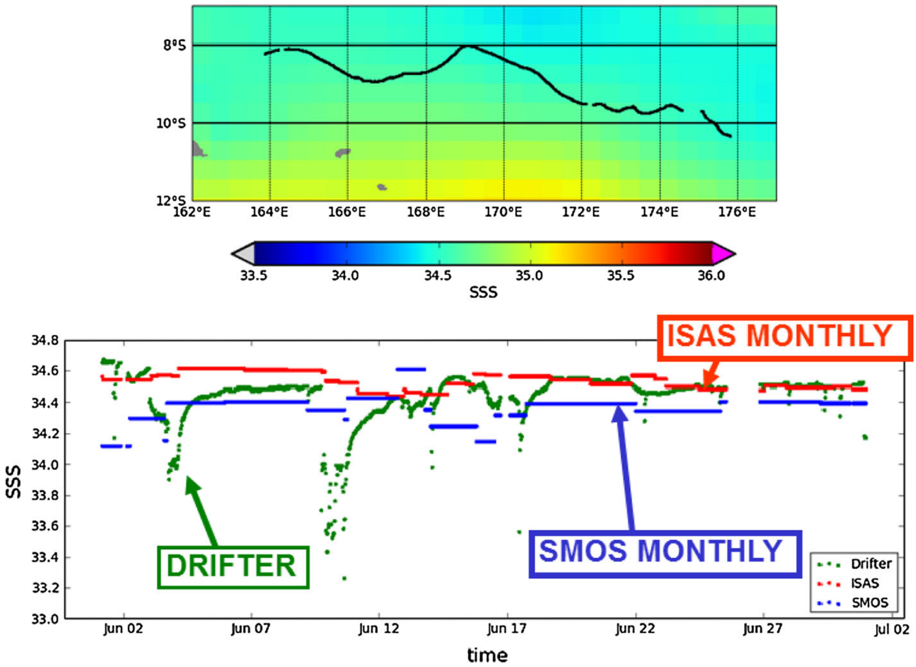

Fig. 23 *Top*: trajectory of a surface velocity program (SVP) float in the western Pacific region measuring conductivity and temperature at 45-cm depth. *Bottom*: SSS along the drifter trajectory measured by the drifter (*green*), derived from SMOS monthly map (*blue*), from ISAS monthly map (*red*)

5 Fresh Pool Interactions with Wind-driven Processes

In this section, two specific SMOS observation cases of wind-driven phenomena are presented. The first example illustrates the erosion of the Far Eastern Pacific Fresh Pool by the gap-wind-driven Panama upwelling processes, whereas the second focuses on the salty wake left behind hurricanes after their passing over the Amazon–Orinoco river plumes.

5.1 An Example of Fresh Pool Erosion by Wind-driven Upwelling

The eastern tropical Pacific Ocean between about 120°W and South America is unique in many respects. Lying in an environment predominantly influenced by the south and northeastern trades and the doldrums, and seasonally affected by the winds from the Caribbean, this region is characterized by complicated and large seasonal variations in the wind field, current pattern, temperature and salinity structure.

The region exhibiting the lowest SSS of the tropical Pacific Ocean, the Eastern Pacific Fresh Pool (EPFP), is found between the warm pool characterized by a mean sea SST greater than 28 °C centered on 15°N along the coast of Central America and the cold and fresh equatorial region, with SSS values lower than 33 pss off the Panama isthmus and lower than 34 pss extending as far as 130°W from the equator to 15°N (Fig. 24).

The EPFP reflects both the conditions of excess precipitation over evaporation beneath the ITCZ and inputs of freshwater from the Andes and Caribbean regions (Benway and Mix 2004). Analysis of a recent gridded in situ SSS product (Delcroix et al. 2011) points out that interannual variations are relatively weak in the EPFP but that seasonal variations are the strongest within the tropical Pacific. Large-scale analysis suggests that the SSS seasonal balance is mostly driven by precipitation in the part of the EPFP covered by the ITCZ, but more complex in the far east as advection and entrainment become important processes (Bingham et al. 2010; Alory et al. 2012).

By focusing on seasonal SSS variations along a well-sampled Voluntary Observing Ship (VOS) line from Panama to Tahiti, Alory et al. (2012) recently showed that this fresh pool dynamically responds to strong regional ocean–atmosphere–land interactions. First, monsoon rains (and associated river runoff) give birth to the fresh pool in the Panama Bight during summer and fall. Second, strong currents driven by topography-induced winds extend the pool westward in winter, while it eventually disappears by mixing with upwelled saltier waters to the east. These dynamic features also generate steep SSS fronts at the edges of the fresh pool (sometimes larger than $\sim$4 pss/° of longitude at the eastern edges).

These SSS fronts and the amplitude of their seasonal cycle are large enough to be detected by the new SMOS satellite mission. Compared to in situ data, SMOS satellite data provide a more homogeneous coverage with finer spatial resolution. Examples of SMOS SSS maps averaged over 10 days and centered at selected dates in December 2010, February and April 2011 are presented in Fig. 24. Remarkably, all the major features observed with in situ VOS data as detailed in Alory et al. (2012) are well reproduced in the SMOS analysis, notably the westward expansion of the fresh pool (SSS $<$ 33 pss) from 85°W in December to 95°W in April, the steep SSS front east of the 32 pss isohaline and SSS minimum of 28 pss in the Panama Bight in December, and the strong SSS increase to around 35 pss in the Panama Bight in April. Moreover, SSS changes occurring between December and April are qualitatively consistent with the expected effects of winter climatological currents, including the Panama Bight upwelling.

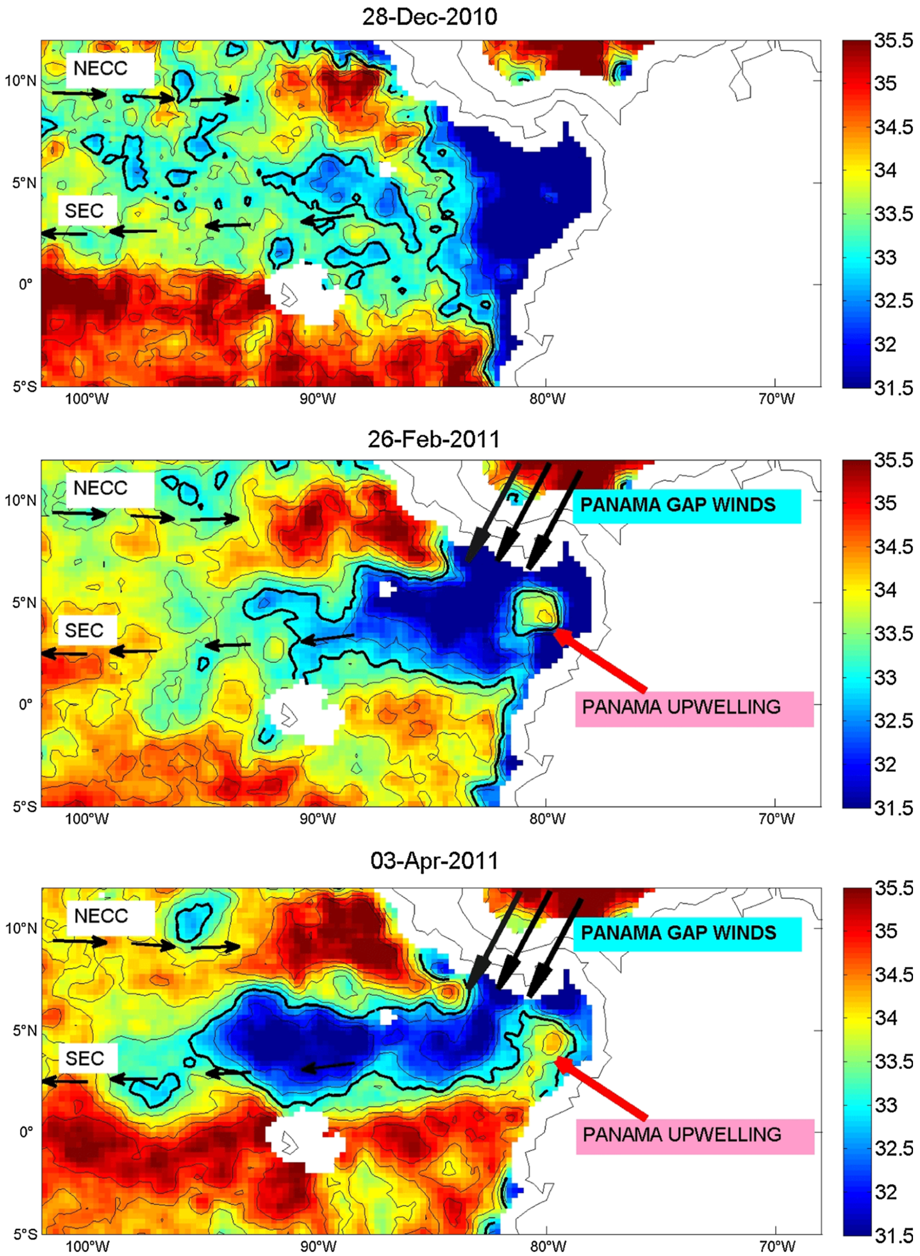

Fig. 24 10-Day averaged SMOS SSS fields centered on the December 28, 2010 (*top*), February 16, 2011 (*middle*), and April 3, 2011 (*bottom*). *Small black arrows* indicate the major surface currents, namely the south equatorial current (SEC) and NECC. *Thick black contour* is indicating the 32 pss isohaline

The freshwater pool disruption as observed by SMOS in the Panama Bight (Fig. 24, middle and bottom panels) is associated with the following processes: during the boreal winter, as the ITCZ moves southward, the northeasterly Panama gap wind creates a southwestward jet-like current in its path with a dipole of Ekman pumping/eddies on its flanks. As a result, upwelling in the Panama Bight brings cold and salty waters to the surface that erode the fresh pool on its eastern side while surface currents stretch the pool westward.

Interestingly, SMOS data are also able to detect other meso-scale features in the region around the fresh pool such as the near-equatorial SSS front or the local SSS maximum in the Costa Rica dome.

Therefore, SMOS SSS data will help in exploring qualitatively the seasonal dynamics of the fresh pools from their birth to their final erosion by wind-driven and turbulent processes (surface current stirring and wind-driven upwelling). Quantifying the relative contribution of the different mechanisms on SSS variations would require a model-based synergetic data analysis scheme to establish the mixed layer salt budget. Also, the regional occurrence of SSS fronts and barrier layers (de Boyer Montégut et al. 2007) suggests, by analogy with the western tropical Pacific, a link between surface and subsurface salinity which could give additional value to the satellite SSS data (Maes 2008; Bosc et al. 2009). As barrier layers can play an active role on the tropical climate (e.g., Maes et al. 2002, 2005), studying their impacts in the region seems worthwhile. This could be done through regional modeling combined with the analysis of subsurface/surface in situ and satellite data. Also, interannual variations of the fresh pool, even if quantitatively smaller than its seasonal variations, need further investigation as ENSO is a strong climate driver in the eastern Pacific. Now that 3 years of SMOS data are available, such type of analysis can be initiated.

5.2 Fresh Pool Interactions with Tropical Cyclones

Because of the buoyant plume of freshwater that forms in the Atlantic due to discharge from the Amazon and Orinoco rivers, the northwestern tropical Atlantic is a region where the salt-driven upper ocean stratification may significantly impact ocean–atmosphere interactions under tropical Cyclones. The spreading of the Amazon–Orinoco River plume exhibits a seasonal cycle coinciding with the Atlantic hurricane season (1 June–30 November) with river influenced minimum salinities observed farthest eastward and northwestward during the height of the hurricane season (mid-August to mid-October). As shown by Ffield (2007), for the 1960–2000 time period, 60 and 68 % of all category 4 and 5 hurricanes, respectively, passed directly over the plume region, revealing that the most destructive hurricanes may be influenced by plume–atmosphere interaction just prior to reaching the Caribbean. Historical in situ data reveal that average ocean surface temperatures first encountered by tropical cyclones moving westward between 12° and 20°N is only 26 °C, but upon reaching the northern reaches of the Amazon–Orinoco River plume (e.g., see Fig. 25), the average SST encountered by tropical cyclones are 2 °C warmer. These warm ocean surface temperatures may play a role in hurricane maintenance and intensification since hurricanes can only form in extensive ocean areas with a surface temperature greater than 25.5 deg C (Dare and McBride 2011). In addition, as shown by Ffield (2007), the buoyant, and therefore stable, 10- to 60-m-thick layer of the plume can mask the presence and influence of other ocean processes and features just below the plume, in particular cool (during hurricane season) surface temperatures carried by NBC rings. After shedding from the NBC retroflection, the 300–500-km-diameter anticyclonic (clockwise) NBC rings pass northwestward through the Amazon–Orinoco River plume toward the Caribbean. The limited observations reveal that at times the cool upper-layer temperatures of the NBC rings are exposed to the atmosphere, while at other times, they are hidden just underneath warm plume water. Strong winds from the 300–1,000-km-diameter cyclonic (counterclockwise) hurricanes might quickly erode a thin plume, exposing several degrees-cooler NBC ring water to the surface, and potentially contributing to limit further development of hurricanes. As shown by Ffields (2007), the warm temperatures associated with the low-salinity Amazon–Orinoco River plume and the relatively cool temperatures associated with NBC rings are in close proximity to the passing hurricanes. As such, they are expected to actively influence the hurricane maintenance and intensification although the interaction is challenging to accurately quantify.

Vizy and Cook (2010) more recently studied the atmospheric response of the summertime large-scale climate to the Amazon/Orinoco plume sea surface temperature anomaly forcing using a regional climate model. They performed simulations in the presence or absence of the Amazon/Orinoco plume SST anomalies. Results from their simulations indicate that the plume does significantly influence the frequency and intensity of summertime storm systems over the Atlantic, consistent with Ffield (2007). The presence of the plume increases the average number of Atlantic basin storms per summer by 60 %. An increase in storm intensity also occurs, with a 61 % increase in the number of storms that reach tropical storm and hurricane strength. Results from their simulations suggest that Atlantic storms also tend to curve northward further west in the Atlantic basin in the presence of the plume SST anomaly. These results support the premise that the warm and low-salinity combined Amazon–Orinoco River plume play an important role in modulating the air–sea interaction during hurricane passages in a manner similar to persistent freshwater barriers layers.

For instance, when there is a freshwater barrier layer, such as in the northwestern tropical Atlantic, mixing is restricted within shallower mixed layer and entrainment of cool thermocline water into the mixed layer is reduced (e.g., Anderson et al. 1996; Vialard and Delecluse 1998a, b; Foltz and McPhaden 2009). As discussed in Price (2009), if the net salinity anomaly (freshwater layer thickness times salinity anomaly in the initial state) is as

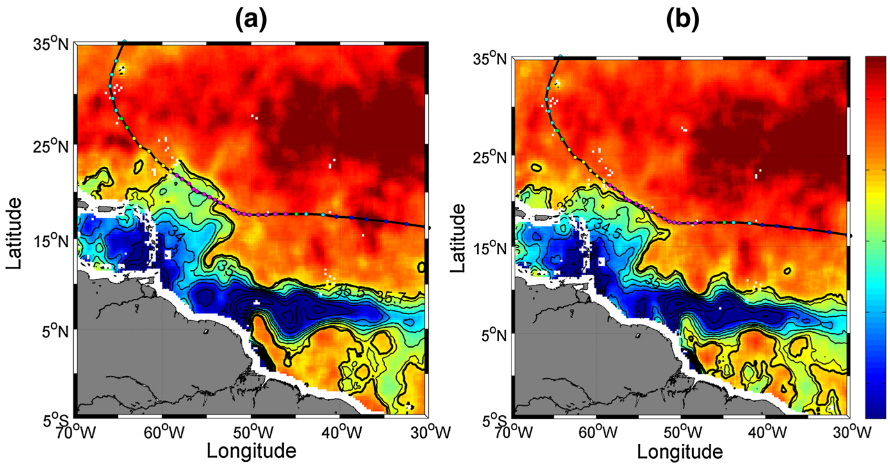

Fig. 25 Two SMOS microwave satellite-derived SSS composite images of the Amazon plume region revealing the SSS conditions **a** before and **b** after the passing of Hurricane Igor, a category 4 hurricane that attained wind speeds of 136 knots in September 2010 during its passage over the plume. *Color-coded circles* mark the successive hurricane eye positions. Seven days of data centered on **a** September 10, 2010 and **b** September 22, 2010 have been averaged to construct the SSS images, which are smoothed by a 1° × 1° block average

large as about 20 m, then the fresh layer will potentially inhibit vertical mixing significantly. As the freshwater surface layer (halocline) of the Amazon and Orinoco river plumes is warmer than the water below (Ffield 2007), salinity stratification acts to reduce the depth of vertical mixing and thus sea surface cooling. The reduced cooling amplitude in the wake of hurricanes passing over the Amazon and Orinoco river plumes, associated with thick barrier layer (BL) effects, might be an important mechanism in favor of hurricane intensification in that region. Similar impact of barrier layers on TC-induced sea surface cooling has been recently evidenced for several case studies such as in the tropical Atlantic (Balaguru et al. 2012), in the Bay of Bengal (Yu and McPhaden 2011; Neetu et al. 2012) and in the tropical Northwest Pacific (Wang et al. 2011).

New insight into the interactions between such extreme atmospheric events and large-scale fresh pools at the ocean surface has been gained from the satellite-based SSS observations as recently reported by Grodsky et al. (2012). They used data from the Aquarius/SAC-D and SMOS satellites to help elucidate the ocean response to hurricane Katia, which crossed the Amazon plume in early fall 2011. As illustrated in their paper, the Katia passage left a 1.5 pss high haline wake covering $>10^5$ km^2 (in its impact on density, the equivalent of a 3.5 °C cooling) due to mixing of the shallow BL.

As illustrated in Fig. 25, very similar observations were also detected from SMOS data alone during the passage of the Category 4 hurricane Igor over the river plume in 2010. The data evidence an erosion of the thin northern reach of the plume fresh surface layer by Igor hurricane-induced mixing, covering an area of $\sim$89,000 km^2 located on the storm right-hand side, where SSS increases by $\sim$1 practical salinity scale while SST cools by 2–3 °C (not shown). On the left side of the storm, much smaller SSS and SST changes are detected after the storm passage. The strong SSS increase in the hurricane wake within the plume is explained by the erosion of the BL. This is supported by Argo profiles collected within the plume (see Grodsky et al. 2012). Mixed layer salinity is lower by 2–4 pss than the water beneath. The shallow haline stratification is destroyed by hurricane-forced entrainment which is stronger on the right side of hurricane eye (Price 2009). It results in a strong SSS signal. Although the hurricane strengthened further along the trajectory, the SSS change is much weaker there corresponding to weak vertical salinity stratification outside the plume.

As further discussed in Grodsky et al. 2012, the fresh (more buoyant) BL limits the turbulent mixing and then the SST cooling in the plume, and thus preserved higher SST and freshwater evaporation than outside. Combined with SST, the new satellite SSS data thus provide a new and better tool to monitor the plume extent and quantify the upper ocean responses to tropical cyclones with important implications for hurricane forecasting.

6 Conclusions and Perspectives

The ocean is the primary return conduit for water transported by the atmosphere. It is the dominant element of the global water cycle, and clearly one of the most important components of the climate system, with more than 1,100 times the heat capacity of the atmosphere. Two new satellite sensors, the ESA SMOS and the NASA Aquarius SAC-D missions, are now providing the first space-borne measurements of the SSS. Synergetic analyses of the new surface salinity data sets together with sea surface temperature, dynamic height and surface geostrophic currents from altimetry, near-surface wind, ocean color, in situ observations, and rainfall estimates will certainly help clarify the freshwater budget in key oceanic tropical areas.

In this paper, we selected illustrative examples to review how the first SSS products derived from the SMOS sensor can readily help to better characterize some of the key processes of the marine branch of the global hydrological cycle. First, we illustrated the new monitoring capabilities for some of the world's largest oceanic freshwater pools generated by the discharge of very large tropical rivers. In particular, we show how SMOS SSS traces the freshwater signals from the Amazon–Orinoco and Congo river plumes. River runoff is an important variable in oceanography as their freshwater affects SSS and the buoyancy of the surface layer, and they represent a source of materials exotic to the ocean and highly important to biological activity. Obviously, they are key hydrologic components of the freshwater exchanges between the atmosphere, land, and ocean. Despite this importance, tracing river freshwater transport over large distances has not been straightforward previously principally because of a lack of SSS data. Tracing those very large rivers over great distances now become an important endeavor, as sufficient data are available from the SMOS and Aquarius sensors that can be further combined with satellite-derived surface geostrophic current data.

Second, we evidenced key oceanic precipitation signatures in the SMOS SSS signal. Satellite radiometry at L-band provides for the first time a global measure of the salinity at the ocean–atmosphere interface (within the upper centimeters). Rain events induce freshening of the ocean surface and are responsible for a high temporal variability in the SSS, consistently detected by both in situ and space-borne sensors. Because of the vertical haline gradient generated by the rain-induced freshening in the upper ocean, fresher surface waters are, however, systematically found from space in rainy area compared with the 1–10-m depth in situ data. These differences challenge calibration/validation activities of the satellite SSS in high precipitation regions. Nevertheless, satellite SSS data certainly provide new information about ocean–atmosphere interfacial freshwater fluxes in these conditions. This was evidenced by comparing spatial patterns and amplitudes of the large-scale SSS anomalies estimated from the SMOS data and the net evaporation minus precipitation fluxes in the tropical Atlantic. Under the Inter Tropical Convergence Zone and sufficiently far away from the river runoff signals, residual SSS anomalies were shown to be highly correlated with the Evaporation minus Precipitaion (E–P) anomalies. In particular, SSS anomalies become increasingly negative as the precipitation anomalies progressively exceed the evaporation anomalies. This demonstrate the importance of monitoring SSS from space in rainy regions, suggesting that the interfacial SSS values might be a good large-scale oceanic rain gauge of the global hydrological water cycle.

The interfacial character of the space-borne measurements also offers new information of interest for ocean circulation models in the perspective of better constraining oceanic precipitation forcing terms.

Finally, the SSS observations from SMOS satellite were used to reveal new aspects of the main tropical fresh pool evolution and interaction with wind-driven atmospheric processes. SMOS imagery thus captures how the large eastern Pacific fresh pool is systematically eroded at the end of the boreal summer on its eastern side by the wind-driven Panama upwelling, which brings cold and salty waters to the surface. Prior to SMOS data availability, the few existing studies of the eastern Pacific describing seasonal variations of SSS did not investigate their cause beyond rainfall (e.g., Fiedler and Talley 2006). Thanks to the new SMOS data, SSS variability associated with wind-driven processes in that region, such as the Panama upwelling signal recently evidenced by Alory et al. (2012), can now be characterized more deeply.

Because of the buoyant character of the freshwater that forms at the ocean surface due to large river discharges or intense local precipitation, the upper ocean stratification in several key tropical oceans regions (e.g., northwestern tropical Atlantic, eastern and western Pacific fresh pools, Bay of Bengal) is mostly controlled by salinity. In such freshwater pool regions, a uniform density mixed layer is found to form the so-called Barrier Layers (BL) at shallower depth than the uniform temperature layer. Because of stable halocline, the BL are acting to inhibit surface cooling and vertical mixing under the action of surface wind stresses. Therefore, there can be some feedback mechanisms between atmospheric, or terrestrial, freshwater fluxes to the ocean and intense atmospheric processes. About 68 % of hurricanes that finally reached category 4 and 5 have thus crossed the Amazon/Orinoco plume (Ffield 2007) where the presence of Barrier Layers can enhance their growth rate by 50 % (Balaguru et al. 2012). Under an intense hurricane, the halocline, which is above the thermocline, is first mixed. This produces a SSS wake that is by a few pss saltier than initial SSS in the plume. By analyzing SMOS SSS data before and after the passage of several intense hurricanes over the Amazon River plume in 2010 and 2011, SSS changes >1 pss over areas exceeding 10^5 km^2 were detected. These abrupt changes have implications for SSS climate, since SSS is more long-lived and not damped like SST. In addition, destruction of the BL is apparently associated with a decreased SST cooling in the plume that, in turn, preserves higher SST and evaporation than outside the BL. This difference in SST cooling is explained by additional work required to mix the BL. Thus, BL leads to a reduction in hurricane-induced surface cooling that favors hurricane intensification, as the resulting elevated SST and high evaporation enhance the hurricane's maximum potential intensity. The geographic location and seasonality of the Amazon/Orinoco plume make hurricane overpasses a frequent occurrence. Indeed, the expansion of the plume in August–September coincides with the peak of the production of Cape Verde hurricanes, which includes many of the most intense (category 4–5) hurricanes. Thus, the results presented here strongly suggest that the role of the salinity stratification in mixed layer dynamics should be taken into account when forecasting tropical cyclone growth over freshwater pools that are generating thick BL (Amazon plume, Bay of Bengal, eastern and western Pacific fresh pools). The availability of satellite SSS from Aquarius and SMOS along with in situ Argo measurements is critical to making such model improvements practical.

Acknowledgments Work presented in this paper was partly done under ESA support in the context of the development of the SMOS level 2/Expert Support Laboratory, ESA Support to Science Element SMOS + SOS and SMOS + STORM projects. CNES also partly funded these activities in the frame of the Centre Aval de Traitement des Données SMOS (CATDS) and of the SMOS/ESA GLOSCAL Cal/Val projects. We are indebted to Micha Rijkenberg (Koninklijk Nederlands Instituut voor Onderzoek der Zee Department of Biological Oceanography (BIO)) for giving us access to the Geotraces Leg 2 CTD data, to F. Gaillard (LPO/IFREMER) for providing ISAS maps version 6 (see http://wwz.ifremer.fr/lpo/SO-Argo/Products/Global-Ocean-T-S). Gilles Reverdin (LOCEAN/CNRS) is responsible for French salinity drifter deployment program; he supervised the quality control of these drifter data set and is warmly acknowledged. These data are available on www.locean-ipsl.upmc.fr/smos/drifters. We thank Nicolas Martin for data processing. We are also indebted to JéromeVialard, Matthieu Lengaigne and Emmanuel Vincent for their very helpful comments about SSS variability in the tropical Indian Ocean and about tropical cyclones interactions with the Amazon plume, Thierry Delcroix about SSS variability in the tropical Pacific Ocean. SSM/I data have been processed by Remote Sensing System (www.ssmi.com). The global ocean heat flux and evaporation products were provided by the WHOI OAFlux project (http://oaflux.whoi.edu) funded by the NOAA Climate Observations and Monitoring (COM) program. We thank the two anonymous referees and Doug Vandemark for their very useful comments and detailed corrections, which were very constructive and which helped us to improve our paper.

References

Alory G, Maes C, Delcroix T, Reul N, Illig S (2012) Seasonal dynamics of sea surface salinity off Panama: the far eastern Pacific fresh pool. J Geophys Res 117:C04028

Anderson SP, Weller RA, Lukas R (1996) Surface buoyancy forcing and the mixed layer of the western Pacific warm pool: observations and 1D model results. J Clim 9:3056–3085

Baklouti M, Devenon JL, Bourret A, Froidefond JM, Ternon JF, Fuda JL (2007) New insights in the French Guiana continental shelf circulation and its relation to the North Brazil Current retroflection. J Geophys Res 112:C02023

Balaguru KP, Saravanan SR, Leung LR, Xu Z, Li M, Hsieh JS (2012) Ocean barrier layers' effect on tropical cyclone intensification. PNAS. doi:10.1073/pnas.1201364109

Banks CJ, Gommenginger CP, Srokosz MA, Snaith HM (2012) Validating SMOS ocean surface salinity in the Atlantic with Argo and operational ocean model data. IEEE Trans Geosci Remote Sens 50:1688–1702

Benway HM, Mix AC (2004) Oxygen isotopes, upper-ocean salinity, and precipitation sources in the eastern tropical Pacific, Earth Planet. Sci Lett 224:493–507

Binet D, Marchal E (1993) The large marine ecosystem of shelf areas in the Gulf of Guinea: long-term variability induced by climatic changes. In: Sherman K et al (eds) Large marine ecosystems: stress, mitigation, and sustainability. American Association for the Advancement of Science, Washington, pp 104–118

Bingham FM, Foltz GR, McPhaden MJ (2010) Seasonal cycles of surface layer salinity in the Pacific Ocean. Ocean Sci 6:775–787

Blough NV, Del Vecchio R (2002) Chromophoric DOM in the coastal environment. In: Hansell DA, Carlson CA (eds) Biogeochemistry of marine dissolved organic matter. Academic, San Diego, pp 509–546

Bonjean F, Lagerloef GSE (2002) Diagnostic model and analysis of the surface currents in the tropical Pacific Ocean. J Phys Oceanogr 32:2938–2954

Bornhold BD (1973) Late quaternary sedimentation in the eastern Angola Basin. Massachusetts Institute of Technology, pp 1–213 (thesis)

Bosc C, Delcroix T, Maes C (2009) Barrier layer variability in the western Pacific warm pool from 2000 to 2007. J Geophys Res 114:C06023

Boutin J, Martin N, Yin X, Reul N, Spurgeon P (2012a) First assessment of SMOS data over open Ocean: part II-sea surface salinity. IEEE Trans Geosci Remote Sens 50(5) Part 1: 1662–1675

Boutin J, Martin N, Reverdin G, Yin X, Gaillard F (2012b) Sea surface freshening inferred from SMOS and Argo salinity: impact of rain. Ocean Sci Discuss 9:3331–3357

Boyer TP, Levitus S (2002) Harmonic analysis of climatological sea surface salinity. J Geophys Res 107(C12):8006

Braga ES, Andrie C, Bourles B, Vangriesheim A, Baurand F, Chuchla R (2004) Congo river signature and deep circulation in the eastern Guinea Basin. Deep Sea Res Part I Oceanogr Res Papers 51(8):1057–1073

Cherubin LM, Richardson PL (2007) Caribbean current variability and the influence of the Amazon and Orinoco freshwater plumes. Deep Sea Res Part I Oceanogr Res Papers 54(9):1451–1473

Conmy RN, Coble PG, Cannizzaro JP, Heil CA (2009) Influence of extreme storm events on West Florida shelf CDOM distributions. J Geophys Res 114:G00F04

Cravatte S, Delcroix T, Zhang D, McPhaden MJ, Leloup J (2009) Observed freshening and warming of the western Pacific warm pool. Clim Dyn 33:565–589

Dare RA, McBride JL (2011) The threshold sea surface temperature condition for tropical cyclogenesis. J Clim 24:4570–4576

De Boyer Montégut C, Mignot J, Lazar A, Cravatte S (2007) Control of salinity on the mixed layer depth in the world ocean: 1. General description. J Geophys Res 112:C06011

Del Vecchio R, Subramaniam A (2004) Influence of the Amazon River on the surface optical properties of the Western Tropical North Atlantic Ocean. J Geophys Res 109:C11001

Delcroix T, Alory G, Cravatte S, Corrège T, McPhaden MJ (2011) A gridded sea surface salinity data set for the tropical Pacific with sample applications (1950–2008). Deep Sea Res Part I 58(1):38–48

DeMaster DJ, Smith W, Nelson DM, Aller JY (1996) Biogeochemical processes in Amazon shelf waters: chemical distributions and uptake rates of silicon, carbon and nitrogen. Cont Shelf Res 16:617–643

Dessier A, Donguy J (1994) The sea-surface salinity in the tropical Atlantic between 10-degrees-S and 30-degrees-N—seasonal and interannual variations (1977–1989). Deep Sea Res Part I Oceanogr Res Papers 41(1):81–100

Dickson RR, Yashayaev I, Meincke J, Turrell W, Dye S, Holfort J (2002) Rapid freshening of the deep North Atlantic Ocean over the past four decades. Nature 416:832–837

D'Sa EJ, Hu C, Muller-Karger FE, Carder KL (2002) Estimation of colored dissolved organic matter and salinity fields in case 2 waters using SeaWiFS: examples from Florida Bay and Florida Shelf. J Earth Syst Sci 111:197–207

Durack PJ, Wijffels SE, Matear RJ (2012) Ocean salinities reveal strong global water cycle intensification during 1950 to 2000. Science 336:455–458
Eisma D, Van Bennekom AJ (1978) The Zaire River and estuary and the Zaire outflow in the Atlantic Ocean. Neth J Sea Res 12(3/4):255–272
Ferrari GM, Dowell MD (1998) CDOM absorption characteristics with relation to fluorescence and salinity in coastal areas of the southern Baltic Sea. Estuar Coast Shelf Sci 47:91–105
Ffield A (2005) North Brazil current rings viewed by TRMM microwave imager SST and the influence of the Amazon Plume. Deep Sea Res I 52:137–160
Ffield A (2007) Amazon and Orinoco River plumes and NBC rings: bystanders or participants in hurricane events? J Clim 20:316–333
Fiedler PC, Talley LD (2006) Hydrography of the eastern tropical Pacific: a review. Prog Oceanogr 69(2–4):143–180
Flagg CN, Gordon RL, McDowell S (1986) Hydrographic and current observations on the continental slope and shelf of the western equatorial Atlantic. J Phys Oceanogr 16(8):1412–1429
Foltz GR, McPhaden JM (2009) Impact of barrier layer thickness on SST in the central tropical North Atlantic. J Clim 22:285–299
Font J, Camps A, Borges A, Martín-Neira M, Boutin J, Reul N, Kerr YH, Hahne A, Mecklenburg S (2010) SMOS: the challenging sea surface salinity measurement from space. Proc IEEE 98(5):649–665
Font J, Boutin J, Reul N, Spurgeon P, Ballabrera-Poy J, Chuprin A, Gabarró C, Gourrion J, Guimbard S, Hénocq C, Lavender S, Martin N, Martínez J, McCulloch M, Meirold-Mautner I, Mugerin C, Petitcolin F, Portabella M, Sabia R, Talone M, Tenerelli J, Turiel A, Vergely JL, Waldteufel P, Yin X, Zine X, Delwart S (2013) SMOS first data analysis for sea surface salinity determination. Int J Remote Sens. doi:10.1080/01431161.2012.716541
Froelich PN, Atwood DK, Giese GS (1978) Influence of Amazon River discharge on surface salinity and dissolved silicate concentration in the Caribbean Sea. Deep Sea Res 25(8):735–744
Gaillard F, Autret E, Thierry V, Galaup P, Coatanoan C, Loubrieu T (2009) Quality control of large Argo datasets. J Atmos Ocean Tech 26:337–351
Garzoli SL, Ffield A, Johns WE, Yao Q (2004) North Brazil current retroflection and transports. J Geophys Res 109:C01013
Goni GJ, Johns W (2001) A census of North Brazil current rings observed from T/P altimetry: 1992–1998. Geophys Res Let 28(1):1–4
Gordon A, Guilivi CF (2008) Sea surface salinity trends over 50 years within the subtropical North Atlantic. Oceanography 20(1):20–29
Gouriou Y, Delcroix T (2002) Seasonal and ENSO variations of sea surface salinity and temperature in the South Pacific Convergence Zone during 1976–2000. J Geophys Res 107:3185
Grodsky SA, Reul N, Lagerloef G, Reverdin G, Carton JA, Chapron B, Quilfen Y, Kudryavtsev VN, Kao HY (2012) Haline hurricane wake in the Amazon/Orinoco plume: a QUARIUS/SACD and SMOS observations. Geophys Res Lett 39:L20603
Grunseich G, Subrahmanyam B, Murty VSN, Giese BS (2011) Sea surface salinity variability during the Indian Ocean Dipole and ENSO events in the tropical Indian Ocean. J Geophys Res 116:C11013
Hellerman S, Rosenstein M (1983) Normal monthly wind stress over the world ocean with error-estimates. J Phys Oceanogr 13(7):1093–1104
Hellweger F, Gordon A (2002) Tracing Amazon River water into the Caribbean Sea. J Marine Res 60:537–549
Hisard P (1980) Observation de réponses de type “El Niño” dans l’Atlantique tropical oriental, Golfe de Guinée. Oceanol Acta 3:69–78
Hu C, Montgomery ET, Schmitt RW, Muller-Karger FE (2004) The dispersal of the Amazon and Orinoco River water in the tropical Atlantic and Caribbean Sea: observation from space and S-PALACE floats. Deep Sea Res Part II 51:1151–1171
Johns WE, Lee TN, Schott FA, Zantopp RJ, Evans RH (1990) The north Brazil current retroflection: seasonal structure and eddy variability. J Geophys Res 95:22103–22120
Katsaros KB, Buettner KJK (1969) Influence of rainfall on temperature and salinity at the Ocean surface. J Appl Meteorol 8:15–18
Kerr Y, Waldteufel P, Wigneron JP, Delwart S, Cabot F, Boutin J, Escorihuela MJ, Font J, Reul N, Gruhier C (2010) The SMOS mission: new tool for monitoring key elements of the global water cycle. Proc IEEE 98(5):666–687
Klein LA, Swift CT (1977) Improved model for dielectric constant of seawater at microwave frequencies. IEEE Trans Antennas Propag 25:104–111
Koleshnikov AG (1973) Equalant I and Equalant II, physical oceanography. UNESCO Paris 1:1–289

Lagerloef GSE (2012) Satellite mission monitors Ocean surface Salinity. Eos Trans AGU 93(25):233. doi:10.1029/2012EO250001

Lagerloef GSE, Mitchum G, Lukas R, Niiler P (1999) Tropical Pacific near surface currents estimated from altimeter, wind and drifter data. J Geophys Res 104:23313–23326

Lagerloef GSE, Colomb FR, Le Vine D, Wentz F, Yueh S, Ruf C, Lilly J, Gunn J, Chao Y, deCharon A, Feldman G, Swift C (2008) The Aquarius/SAC-D mission: designed to meet the salinity remote-sensing challenge. Oceanography 21(1):68–81

Lagerloef GSE, Boutin J, Chao Y, Delcroix T, Font J, Niiler P, Reul N, Riser S, Schmitt R, Stammer D, Wentz F (2010) Resolving the global surface salinity field and variations by blending satellite and in situ observations, Oceanobs'09: sustained Ocean observations and information for society, Venise, Italy, 21–25 September 2009, ESA Publication WPP-306

Lefèvre N (2009) Low C02 concentrations in the gulf of guinea during the upwelling season in 2006. Mar Chem 113(1–2):93

Lentz SJ (1995) Seasonal-variations in the horizontal structure of the Amazon plume inferred from historical hydrographic data. J Geophys Res 100(C2):2391–2400

Lentz SJ, Limeburner R (1995) The Amazon River Plume during AMASSEDS: spatial characteristics and salinity variability. J Geophys Res 100:2355–2375

Maes C (2008) On the ocean salinity stratification observed at the eastern edge of the equatorial Pacific warm pool. J Geophys Res 113:C03027

Maes C, Picaut J, Belamari S (2002) Salinity barrier layer and onset of El Niño in a Pacific coupled model. Geophys Res Lett 29(24):2206

Maes C, Picaut J, Belamari S (2005) Importance of salinity barrier layer for the buildup of El Niño. J Clim 18:104–118

Meade RH, Nordin CF, Hernandez DP, Mejia A, Godoy JMP (1983) Sediment and water discharge in Rio Orinoco, Venezuela and Colombia. In: Proceedings of the 2nd international symposium on river sedimentation. Water Resources and Electric Poers Press, Beijing, China, pp 1134–1144

Mecklenburg S, Drusch M, Kerr YH, Font J, Martin-Neira M, Delwart S, Buenadicha G, Reul N, Daganzo-Eusebio E, Oliva R, Crapolicchio R (2012) ESA's soil moisture and Ocean salinity mission: mission performance and operations. IEEE Trans Geosci Remote Sens 50(5) Part 1:1354–1366

Merle J (1980) Variabilité thermique annuelle et interannuelle de l'océan Atlantique équatorial est. L'hypothèse d'un " El Niño " Atlantique. Oceanol Acta 3:209–220

Meulenbergh J (1968) Diffusion des eaux du fleuve Congo dans les eaux de l'Atlantique Sud. Acad R Sci Outre Mer Bruxelles 16(6):148

Meybeck M, Ragu A (1997) River discharges to the oceans: an assessment of suspended solids, major ions, and nutrients. IAHS Publ 243:1–245

Michel S, Chapron B, Tournadre J, Reul N (2007) Sea surface salinity variability from a simplified mixed layer model of the global ocean. Ocean Sci Discuss 4:41–106

Mignot J, de Boyer Montégut C, Lazar A, Cravatte S (2007) Control of salinity on the mixed layer depth in the world ocean: 2. Tropical areas. J Geophys Res 112:C10010

Miller R, Zepp RG (1995) Photochemical production of dissolved inorganic carbon from terrestrial organic matter: significance to the oceanic organic carbon cycle. Geophys Res Lett 22:417–420

Milliman JD, Meade RH (1983) World-wide delivery of river sediment to the oceans. J Geol 91(1):1–21

Molleri GSF, de Novo EMLM, Kampel M (2010) Space-time variability of the Amazon River plume based on satellite ocean color. Cont Shelf Res 30(3–4):342–352

Moran MA, Sheldon WM, Sheldon JE (1999) Biodegradation of riverine dissolved organic carbon in five estuaries of the southeastern United States. Estuaries 22:55–64

Morrow R, Valladeau G, Sallee J-B (2008) Observed subsurface signature of Southern Ocean sea level rise. Prog Oceanogr 77(4):351–366

Muller-Karger FE, McClain CR, Richardson PL (1988) The dispersal of the Amazon's water. Nature 333:56–59

Muller-Karger FE, McClain CR, Fisher TR, Esaias WE, Varela R (1989) Pigment distribution in the Caribbean Sea: observations from space. Prog Oceanogr 23:23–64

Muller-Karger FE, Richardson PL, McGillicuddy D (1995) On the offshore dispersal of the Amazon's plume in the North Atlantic. Deep Sea Res Part I 42:2127–2137

Neetu S, Lengaigne M, Vincent EM, Vialard J, Madec G, Samson G, Ramesh Kumar MR, Durand F (2012) Influence of upper-ocean stratification on tropical cyclones- induced surface cooling in the Bay of Bengal. J Geophys Res 117:C12020

Neumann G (1969) Seasonal salinity variations in the upper strata of the western tropical Atlantic ocean-I. Sea surface salinities. Deep Sea Res 16:165–177

Nittrouer CA, Demaster DJ (1986) Sedimentary processes on the Amazon continental shelf: past, present and future research. Cont Shelf Res 6:5–30
Obernosterer I, Herndl GJ (2000) Differences in the optical and biological reactivity of the humic and non-humic DOC component in two contrasting coastal marine environments. Limnol Oceanogr 45:1120–1129
Ostapoff F, Tarbeyev Y, Worthem S (1973) Heat flux and precipitation estimates from oceanographic observations. Science 180:960–962
Palacios SL, Peterson TD, Kudela RM (2009) Development of synthetic salinity from remote sensing for the Columbia River Plume. J Geophys Res 114:C00B05
Perry GD, Duffy PB, Miller NL (1996) An extended data set of river discharges for validation of general circulation models. J Geophys Res 101:21339–21349
Piterbarg LI, Ostrovskii AG (1997) Advection and diffusion in random media: implications for sea surface temperature anomalies. Kluwer Academic, New York
Piton B, Wacongne S (1985) Unusual amounts of very saline subsurface water in the eastern Gulf of Guinea in May 1984. Tropical Ocean-Atmosphere Newsletter, pp 325–328
Price JF (2009) Metrics of hurricane-ocean interaction: vertically-integrated or vertically- averaged ocean temperature? Ocean Sci 5:351–368
Reul N, Tenerelli J (2011) SMOS level 3 SSS research products—product validation document—reprocessed year 2010. CECOS/CNES/IFREMER/CATDS Techn Doc. Available from www.catds.fr
Reul N, Saux-Picart S, Chapron B, Vandemark D, Tournadre J, Salisbury J (2009) Demonstration of ocean surface salinity microwave measurements from space using AMSR-E over the Amazon plume. Geophys Res Lett 36:L13607
Reul N, Tenerelli J, Boutin J, Chapron B, Paul F, Brion E, Gaillard F, Archer O (2012) Overview of the first SMOS sea surface salinity products. Part I: quality assessment for the second half of 2010. IEEE Trans Geosci Remote Sens 50(5):1636–1647
Reverdin G, Kestenare E, Frankignoul C, Delcroix T (2007) Sea surface salinity in the Atlantic Ocean (30°S–50°N). Prog Oceanogr 73:311–340
Reverdin G, Morisset S, Boutin J, Martin N (2012) Rain-induced variability of near sea- surface *T* and *S* from drifter data. J Geophys Res 117:C02032
Richardson PL, McKee T (1984) Average seasonal variation of the Atlantic equatorial currents from historical ship drifts. J Phys Oceanogr 14(7):1226–1238
Ruf CS, Swift CT, Tanner AB, Le Vine DM (1988) Interferometric synthetic aperture microwave radiometry for the remote sensing of the Earth. IEEE Trans Geosci Remote Sens 26:597–611
Salisbury J, Vandemark D, Campbell J, Hunt C, Wisser D, Reul N, Chapron B (2011) Spatial and temporal coherence between Amazon River discharge, salinity, and light absorption by colored organic carbon in western tropical Atlantic surface waters. J Geophys Res 116:C00H02
Schlössel P, Soloviev A, Emery WJ (1997) Cool and freshwater skin of the ocean during rainfall. Bound Layer Meteorol 82(3):439–474
Schmitt RW(2008) Salinity and the global water cycle. Oceanography 21(1):12–19
Singh A, Delcroix T, Cravatte S (2011) Contrasting the flavors of El Niño-Southern Oscillation using sea surface salinity observations. J Geophys Res 116:C06016
Smith WO, Demaster DJ (1996) Phytoplankton biomass and productivity in the Amazon River plume: correlation with seasonal river discharge. Cont Shelf Res 16(3):291–319
Soloviev A, Lukas R (1996) Observation of spatial variability of diurnal thermocline and rainformed halocline in the Western Pacific warm pool. J Phys Oceanogr 26:2529–2538
Steven DM, Brooks AL (1972) Identification of Amazon River water at Barbados, W. Indies, by salinity and silicate measurements. Mar Biol 14(4):345–348
Ternon JF, Oudot C, Dessier A, Diverres D (2000) A seasonal tropical sink for atmospheric $C0_2$ in the Atlantic Ocean: the role of the Amazon River discharge. Mar Chem 68(3):183–201
Terray L, Corre L, Cravatte S, Delcroix T, Reverdin G, Ribes A (2011) Near-surface salinity as nature's rain gauge to detect human influence on the tropical water cycle. J Clim 25:958–977
Twardowski MS, Donaghay PL (2001) Separating in situ and terrigenous sources of absorption by dissolved material in coastal waters. J Geophys Res 106(C2):2545–2560
UNESCO (1985) The international system of units (SI) in oceanography, UNESCO technical papers no. 45, IAPSO Pub. Sci. No. 32, Paris, France
Van Bennekom AJ, Berger GW (1984) Hydrography and silica Budget of the Angola Basin. Neth J Sea Res 17(2–4):149–200
Van Bennekom AJ, Jager JE (1978) Dissolved aluminium in the Zaire River plume. Neth J Sea Res 12(3/4):358–367

Vangriesheim A, Pierre C, Aminot A, Metzl N, Baurand F, Caprais JC (2009) The influence of Congo river discharges in the surface and deep layers of the gulf of guinea. Deep Sea Res Part II Top Stud Oceanogr 56(23):2183–2196
Vialard J, Delecluse P (1998a) An OGCM study for the TOGA decade. Part I: role of salinity in the physics of the Western Pacific Fresh Pool. J Phys Oceanogr 28:1071–1088
Vialard J, Delecluse P (1998b) An OGCM study for the TOGA decade. Part II: barrier layer formation and variability. J Phys Oceanogr 28:1089–1106
Vizy EK, Cook KH (2010) Influence of the Amazon/Orinoco Plume on the summertime Atlantic climate. J Geophys Res 115:D21112
Vörösmarty CJ, Fekete B, Tucker BA (1998) River discharge database, version 1.1 (RivDIS v1.0 supplement). Institute for the Study of Earth, Oceans, and Space, University of New Hampshire, Durham, NH
Wang X, Han G, Qi Y, Li W (2011) Impact of barrier layer on typhoon-induced sea surface cooling. Dyn Atmos Oceans 52(3):367–385
Wauthy B (1977) Révision de la classification des eaux de surface du golfe de Guinée. Cah Orstom Sér Océanogr 15(3):279–295
Wijesekera HW, Paulson CA, Huyer A (1999) The effect of rainfall on the surface layer during a westerly wind burst in the western equatorial Pacific. J Phys Oceanogr 29:612–632
Wisser D, Fekete BM, Vörösmarty CJ, Schumann AH (2010) Reconstructing 20th century global hydrography: a contribution to the global terrestrial network-hydrology (GTN-H). Hydrol Earth Syst Sci 14:1–24
Yamashita Y, Tanoue E (2004) In situ production of chromophoric dissolved organic matter in coastal environments. Geophys Res Lett 31:L14302
Yin X, Boutin J, Martin N, Spurgeon P (2012) Optimization of L-Band Sea surface emissivity models deduced from SMOS data. IEEE Trans Geosci Remote Sens 50:1414–1426
Yoo JM, Carton JA (1988) Spatial dependence of the relationship between rainfall and outgoing longwave radiation in the tropical Atlantic. J Clim 1:1047–1056
Yu L (2010) On sea surface salinity skin effect induced by evaporation and implications for remote sensing of Ocean salinity. J Phys Oceanogr 40(1):85
Yu L (2011) A global relationship between the ocean water cycle and near-surface salinity. J Geophys Res 116:C10025
Yu L, McPhaden MJ (2011) Ocean pre-conditioning of Cyclone Nargis in the Bay of Bengal: interaction between Rossby waves, surface fresh waters, and sea surface temperatures. J Phys Oceanogr 41:1741–1755
Yu L, Weller RA (2007) Objectively analyzed air-sea heat fluxes (OAFlux) for the global ocean. Bull Am Meteorol Soc 88(4):527–539
Yueh SH, West R, Wilson WJ, Li FK, Njoku EG, Rahmatsamii Y (2001) Error sources and feasibility for microwave remote sensing of ocean surface salinity. IEEE Trans Geosci Remote Sens 39:1049–1060
Zhang Y, Zhang X (2012) Ocean haline skin layer and turbulent surface convections. J Geophys Res 117:C04017